Sound-Side Inundation and Seaward Erosion of a Barrier Island during Hurricane Landfall

Christopher R. Sherwood[1], Andrew C. Ritchie[2], Jin-Si R. Over[1], Christine J. Kranenburg[3], Jonathan A. Warrick[2], Jenna A. Brown[4], C. Wayne Wright[5], Alfredo L. Aretxabaleta[1], Sara L. Zeigler[3], Phillipe A. Wernette[2], Daniel D. Buscombe[6], Christie A. Hegermiller[1†]

[1] U.S. Geological Survey, Woods Hole Coastal and Marine Science Center, Woods Hole, MA.

[2] U.S. Geological Survey, Pacific Coastal and Marine Science Center, Santa Cruz, CA.

[3] U.S. Geological Survey, St. Petersburg Coastal and Marine Science Center, St. Petersburg, FL.

[4] U.S. Geological Survey, Maryland-Delaware-District of Columbia Water Science Center, Dover, DE.

[5] C.W. Wright Consulting, Inc., Tampa, FL.

[6] Marda Science, Contractor to the U.S. Geological Survey.

[†]Current affiliation: SoFar Ocean, San Francisco, CA.

Corresponding author: Christopher Sherwood (csherwood@usgs.gov)

Key Points:

- Wind-driven surge from Pamlico Sound inundated the barrier island of North Core Banks during Hurricane Dorian.
- Seaward-directed flow (outwash) through gaps in the dunes eroded about 18% of the island volume, mostly from antecedent washover deposits.
- This event represents a setback for barrier transgression but has created beneficial habitat for endangered species.

Abstract

Barrier islands are especially vulnerable to hurricanes and other large storms, owing to their mobile composition, low elevations, and detachment from the mainland. Conceptual models of barrier-island evolution emphasize ocean-side processes that drive landward migration through overwash, inlet migration, and aeolian transport. In contrast, we found that the impact of Hurricane Dorian (2019) on North Core Banks, a 36-km barrier island on the Outer Banks of North Carolina, was primarily driven by inundation of the island from Pamlico Sound, as evidenced by storm-surge model results and observations of high-water marks and wrack lines. Analysis of photogrammetry products from aerial imagery collected before and after the storm indicate the loss of about 18% of the subaerial volume of the island through the formation of over 80 erosional washout channels extending from the marsh and washover platform, through gaps in the foredunes, to the shoreline. The washout channels were largely co-located with washover fans deposited by earlier events. Net seaward export of sediment resulted in the formation of deltaic bars offshore of the channels, which became part of the post-storm berm recovery by onshore bar migration and partial filling of the washouts with washover deposits within two months. This event represents a volumetric setback in the overwash/rollover behavior required for barrier transgression, but the new ponds and lowland habitats may provide beneficial habit for endangered species and will likely persist for years.

Plain Language Summary

As sea level rises, barrier islands tend to migrate towards land, helped by storms that move sand from the ocean to the back side. In rarer events, such as Hurricane Dorian (2019), storms can transport sand from the back side to the ocean. Using overlapping photos collected from a plane, we created 3-D elevation maps and stitched-together photo mosaics of North Core Banks, North Carolina, immediately before and after Hurricane Dorian, and then once a month for three months afterwards, to document the erosion and recovery of the beach and barrier island. We found major changes. During the storm, abnormally high water levels in Pamlico and Core Sounds flooded the island and created distinct channels as water drained from the sound side into the Atlantic Ocean. This process, called outwash, moved 18% of the island sand into the ocean over the course of a few hours. The maps also

showed the initial stages of a recovery process, as beach sand was moved by ocean waves and plugged the channels, creating new, and semi-permanent, habitats within the barrier island. Events such as Hurricane Dorian may slow the typical migration process of barrier islands and change the landscape for years to come.

1 Introduction

1.1 Motivation

Barrier islands are valued for their habitats and natural resources, recreational opportunities, high property values (e.g., Conroy and Milosch, 2011; Jin et al., 2015) and role in protecting the mainland from coastal storms (Stone and McBride, 1998; Grzegorzewski et al., 2011). Scientific understanding of their response to storms in the presence of changing climate and rising sea level is important for assessing their vulnerability and making decisions on infrastructure protection and resource management. The long-term survival of barrier islands depends on their ability to migrate upwards and landwards apace with relative sea-level rise (Hoyt, 1967; Godfrey and Godfrey, 1976; Wolinsky and Murray, 2009). That migration depends on transport of sand by three processes: inlet formation and deposition of sand in flood-tidal deltas (Fisher, 1962; Pierce, 1970; Cowell et al., 2003; Leatherman, 1979; Nienhuis and Ashton, 2016; Nienhuis and Lorenzo-Trueba, 2019), overwash (Leatherman, 1979; Leatherman, 1983; Donnelley et al., 2006), and aeolian transport (Hosier and Cleary, 1977; Short and Hesp, 1982; Durán Vinent and Moore, 2014; Hovenga et al., 2019). Note: in this paper, overwash and outwash refer to the hydrodynamic processes, and washover (fans, deposits) and washout (channels, deposits) refers to the morphological products, consistent with Neuendorf et al., (2011). Barrier island transgression – the movement of these sand bodies across the underlying continental platform – occurs on geologic time scales (millennia) through a succession of short-term (days) storm-driven events and longer-term (months and years) landscape evolution driven by aeolian transport and vegetation growth that culminate in net landward island migration.

In addition to driving changes in barrier island morphology and position, storms are also important natural disturbances that create and maintain early successional habitats

used by threatened and endangered species, including shorebirds (e.g., piping plover; *Charadrius melodus*; Cohen et al., 2009, Zeigler et al., 2019), plants (e.g., seabeach amaranth; *Amaranthus pumilus;* Sellars and Jolls, 2007), and sea turtles (Cheloniidae sp.; Garmestani et al. 2000). Low-energy foraging habitats with rich invertebrate assemblages are also critical for waterbirds and shorebirds throughout the annual cycle, providing nutrition during the nesting, migratory, and winter seasons (Perry & Uhler, 1988; NRCS, 2000; Perry et al., 2007; Cohen and Fraser, 2010) Furthermore, connectivity and long-distance interactions among barrier island ecosystems—often through storm-driven movement of sediment, propagules, and nutrients—plays a vital role in maintaining coastal ecosystem form and function (van de Koppel et al., 2015, Liebowitz et al., 2016). Thus, the morphodynamics of barrier islands directly influence coastal ecosystems and the flora and fauna that inhabit them.

Not all coastal processes make positive contributions toward landward migration of barrier islands. For example, storm-driven beach and dune erosion with subsequent offshore sand transport is common (e.g., Vellinga, 1982; Russell, 1993; Splinter and Palmsten, 2012; Splinter et al., 2018). Dune erosion during collision, when waves reach the toe of the dune, is the most common form of coastal erosion and is often accompanied by offshore transport of sand as the beach profile adjusts (Sallenger, 2000; Morton and Sallenger, 2003; Stockdon et al., 2007; Brodie et al., 2019; Itzkin et al., 2021). Although erosion driven by ocean storms temporarily retards landward migration, it may be ultimately offset by positive landward transport during overwash, beach rebuilding, and the longer-term aeolian processes of dune building. In comparison, the offshore transport of large volumes of sand from a barrier island by erosive flows during sound-side inundation is a uniquely different and poorly understood process that is also responsible for setbacks in landward migration of barrier islands. Recent inventories suggest that sound-side inundation and “outwash” events during hurricanes may be more common than previously recognized (Over et al., 2021a). However, the impact of these outwash events on barrier island morphology, morphodynamics, sediment budgets and habitats are unknown. To place these outwash events in the context of barrier island survival, it is important to

quantify the magnitude and patterns of sediment movement and evaluate the prospects and time scales for recovery.

Here we provide the first ever morphodynamic and sediment budget observations of a large outwash event across a barrier island and use these results to characterize both storm and recovery changes. As detailed below, an outwash event flooded across North Core Banks, North Carolina, during the passage of Hurricane Dorian in 2019, and photogrammetry flights using a small airplane were used to characterize the subsequent island evolution. These results are used to address fundamental questions about outwash events, including: What are the patterns and rates of sediment transport during an outwash event? What are the patterns and time scales of recovery following an outwash event? How do these factors differ from more commonly observed ocean-side storm-based erosion events? What are the long-term implications of outwash events to barrier island migration, morphology, and habitats?

1.2 Study area – North Core Banks, Cape Lookout National Seashore

North Core Banks, located in Cape Lookout National Seashore, North Carolina, USA is a narrow (200 – 3,200-m wide), low-lying (mean elevation <2 m NAVD88, highest elevation ~8.5 m NADV88) barrier island on the Outer Banks of North Carolina (Riggs & Ames, 2007). The island is part of a chain extending along Raleigh Bay from Cape Lookout to Cape Hatteras, forming the Ocracoke littoral cell (Inman & Dolan, 1989; Figure 1a). The central and northeastern parts of North Core Banks are wider and higher, with multiple dune lines and hillocks revealing a history of barrier migration. There is minimal infrastructure on the island, including several National Park Service cabins at Long Point, one house near the middle of the island, two small docks on the sound side, and about a dozen historical structures in the village of Portsmouth (abandoned in 1971) at the northeast end. A sand road behind the dunes runs the length of the island with beach access points. The southern end of North Core Banks is defined by shifting and ephemeral inlets.

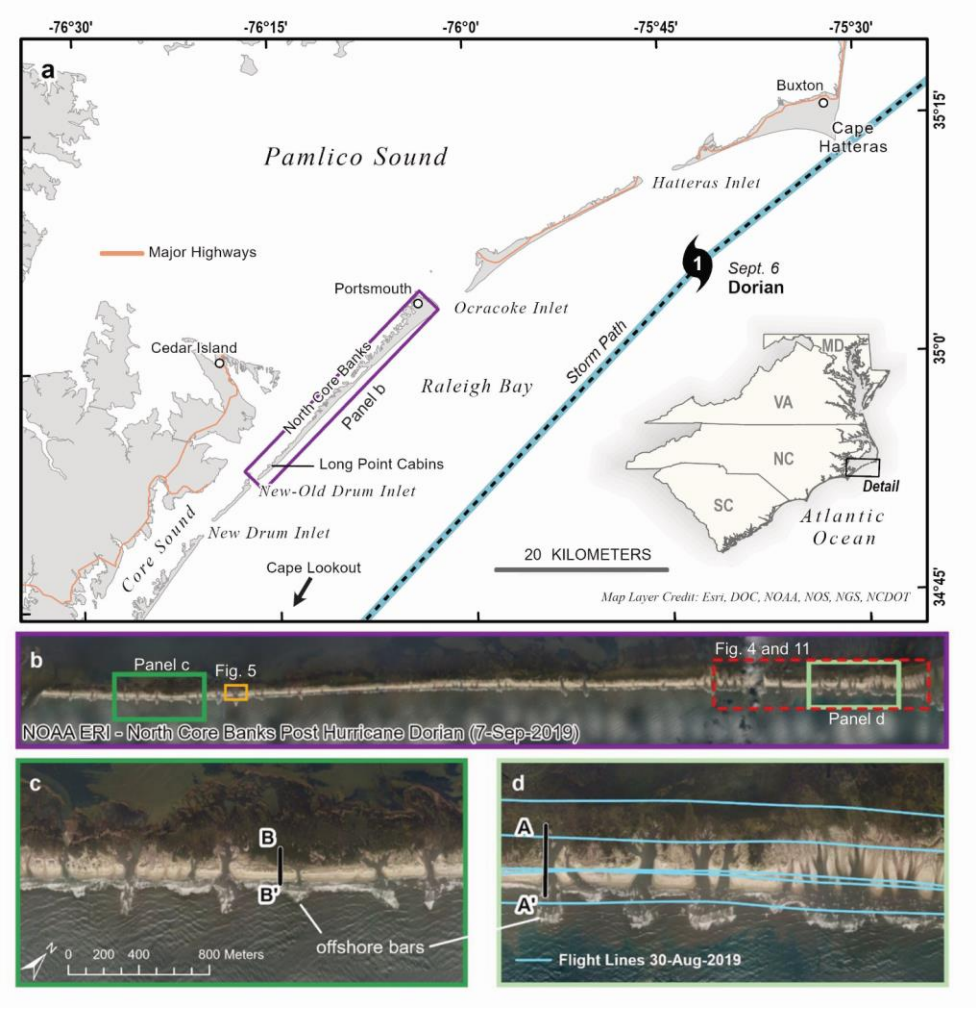

Figure 1. Maps of North Core Banks. a) Track of Hurricane Dorian on September 6, 2019 and box showing the location of panel (b), b) NOAA Emergency Response Imagery taken September 7, 2019 (NGS, 2022) with boxes showing the locations of panels (c) and (d) and Figure, c) detail of washout channels on the southwest end, and d) washout channels on the northeast end near Portsmouth with blue lines indicating flight lines. Note the breaking waves directly offshore of the outwash channels. The red dashed box on (b) is the extent of Figures 4 and 11 and the lines labelled A-A' and B-B' on (c) and (d) are the transect locations of Figure 10.

Our study focused on a 36-km stretch of North Core Banks where the effects of Hurricane Dorian were most evident, bounded by New-Old Drum Inlet to the southwest and by Ocracoke Inlet to the northeast (Figure 1a). New-Old Drum Inlet is located about 2.5 km southwest of the Long Point cabins and was formed during Hurricane Dennis in September 1999 (Riggs & Ames, 2007). The northeastern portion of the study area includes several islands separated by swash inlets (Riggs & Ames, 2007), which are remnants of

earlier inlets with shallow channels that, prior to Hurricane Dorian, did not extend below mean sea level. The largest, highest, and northernmost of these islands is Portsmouth Island, bounded on the north by Ocracoke Inlet. Ocracoke Inlet is the largest in the Core Banks–Ocracoke chain and the oldest inlet on the Outer Banks (Riggs & Ames, 2007; Mallinson et al., 2008). These undeveloped islands support critical nesting, stopover, and/or wintering habitats used by several species listed under the U.S. Endangered Species Act (16 U.S.C. 1531-1544; https://www.fws.gov/media/endangered-species-act), including shorebirds (e.g., piping plovers; red knots, *Calidris canutus rufa*), sea turtles (superfamily Chelonioidea), and seabeach amaranth (*Amaranthus pumilus*).

North Core Banks separates the Atlantic Ocean from Core Sound, a southern extension of Pamlico Sound (Figure 1a). Pamlico Sound, Core Sound, and the Tar-Pamlico and Neuse River estuaries form a broad, shallow estuarine lagoon system that has negligible tides except near tidal inlets but is prone to wind-driven surges that have historically caused sound-side flooding (e.g., Pietrafesa et al., 1997; Peng et al., 2004; Leuttich et al., 2002; Mulligan et al., 2015; Clunies et al., 2017; Cassalho et al., 2021). The ocean tides are microtidal, with a mean range of about 1 m (Hayes, 1979; NOAA Station 8656937) and a mean high-water elevation of ~0.4 m NAVD88 (VDatum; Hess et al., 2005). The mean annual significant wave height on the ocean side is 1.3 m (Mulhern et al., 2017, based on WaveWatch III model results), placing the barrier in the wave-dominated regime (Hayes, 1979). Local relative sea level is rising. Previous estimates of relative sea level rise (SLR) change in the Outer Banks during the late Holocene range from 0.8 to 1.1 $\cdot 10^{-3}$ m y^{-1} (Horton et al., 2009), but recent tide-gauge data from Duck (1978-2020), Oregon Inlet (1977-2020), and Beaufort (1953-2020) indicate rates of 3 – 5 $\cdot 10^{-3}$ m y^{-1} (https://tidesandcurrents.noaa.gov/sltrends/mslUSTrendsTable.html). Estimates of rates and spatial extent of SLR show strong decadal fluctuation (especially prior to 1988) and are highly dependent on the period analyzed (Little et al., 2021).

Late 20th-century observations indicate that the shoreline position of North Core Banks is receding. Spatially averaged shoreline-change rates on the ocean side of North Core Banks, determined from repeat transect measurements between 1961 and 2001, varied between -20 to +6 m y^{-1}, depending on the period of observation. For the longest

period (1946-1998), the rate was -1.3 m y^{-1} (Table 5 in Riggs & Ames, 2007; negative numbers indicate shoreline erosion). Higher rates, as much as -69 m y^{-1}, were observed on individual transects, notably those near transient inlets. Riggs & Ames (2007) report that shoreline movements are accompanied by elevation increases with average rates of about 4 cm y^{-1} that are generally highest near the shore (3 – 6 cm y^{-1}) but decrease to 2 – 5 cm y^{-1} 60 m inland (Table 6 in Riggs & Ames, 2007). Rates vary depending on the location and period of observation; recent observations on the beaches and dunes by Hovenga et al. (2019) found interannual rates of 5 – 11 cm y^{-1}, but multidecadal rates of 2 – 4 cm y^{-1}. Combined, the receding shoreline and increasing beach and dune elevations are consistent with a general landward migration of this barrier island.

North Core Banks experienced extensive overwash during Hurricane Florence, which made landfall at Wrightsville Beach, NC (~180 km southwest of North Core Banks) a year earlier (18 September 2018). USGS aerial imagery (described below) taken eighteen days later (6 November 2018) shows fresh-looking washover fans likely created during Hurricane Florence (Ritchie et al., 2021). These are relevant because of their apparent co-location with the outwash features formed during Hurricane Dorian.

The primary dune line of North Core Banks had an elevation of 3 to 6 m before Hurricane Dorian, with dozens of gaps ~2 - 2.5-m high that served as throats (Donnelly et al., 2006) leading to the Florence washover fans (Lazarus, 2016; Lazarus et al., 2020). Additional cuts through the dunes accommodated sand roads for vehicle access to the beach.

1.3 Hurricane Dorian

Hurricane Dorian made landfall at Cape Hatteras, NC (Figure 1a) on September 6, 2019, as a category 1 storm on the Saffir-Simpson Hurricane Wind Scale after devastating the Bahamas as the strongest storm in modern records (Avila et al., 2020). As the hurricane traversed Raleigh Bay from Cape Lookout to Cape Hatteras, onshore winds from the southeast pushed the waters of Pamlico Sound north and west, flooding the estuaries and creeks with water levels greater than 1.5 m NAVD88 in the Neuse River (https://stn.wim.usgs.gov/FEV/#2019HurricaneDorian, last accessed 8/17/2022). After

landfall at Cape Hatteras, the hurricane moved rapidly offshore. Winds shifted abruptly to come from the northwest and waters surged southward back across Pamlico Sound, into Core Sound, and onto the back barrier of North Core Banks and Ocracoke Island (Figure 2; Figure 3), where water levels of more than 2 m were reported in the town of Ocracoke (https://www.washingtonpost.com/weather/2019/09/06/water-rises-feet-hours-ocracoke-north-carolina-eye-hurricane-dorian-moved-past/, last accessed 8/17/2022). No people or instruments were on the low-lying island of North Core Banks to record this event, but images taken by NOAA during an emergency response flight the next day (Figure 1, Table 1) revealed that the island had been dissected by more than 80 channels cut through the primary dune line as water rushed seaward. This process, termed outwash (Over et al., 2021a), generated an array of both erosional features (washout channels) on the subaerial island and depositional features (washout fans and deltas) in the subtidal nearshore. Piles of wrack lay stranded high on the landward side of the dunes, and small outwash deltas extended into the surf zone from the newly cut channels. These images show that the island was inundated from the sound side, causing significant and potentially long-lasting geomorphic changes (Figure 1b-d).

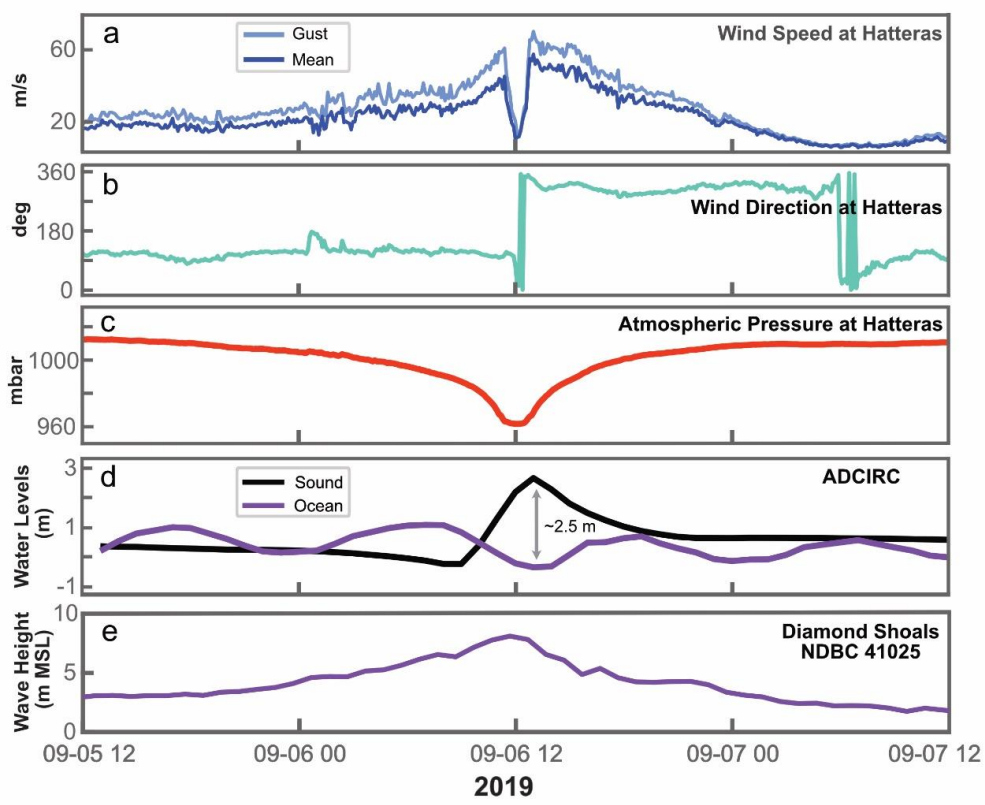

Figure 2. Time series (universal time coordinate; UTC) of meteorological and oceanographic conditions during the passage of Dorian. Wind speed (a), wind direction (b), and barometric pressure (c) at Cape Hatteras. Water levels from the ADCIRC model forecast (d) near N. Core Banks in Pamlico Sound (black) and the Atlantic Ocean (purple). Significant wave height at NDBC buoy 41025, located about 70 km east of North Core Banks in water ~60 m deep. Sources: NOAA station 8654467 at US Coast Guard Station Hatteras, NC; NDBC buoy 41025 (https://tidesandcurrents.noaa.gov/stationhome.html?id=8654467; https://www.ndbc.noaa.gov/station_page.php?station=41025) and ADCIRC model forecasts (adcircprediction.org)

1.4 Objective and Outline

The objective of this paper is to describe the changes wrought by Hurricane Dorian on North Core Banks and put the event into context with better-known morphological processes that shape barrier islands. In doing so, we gain insight into processes that might punctuate the transgression of barriers during periods of sea-level rise. In Section 2 we describe our data sources and analyses, and, in section 3, we present our results. Section 4 is a discussion of these results and the implications of sound-side inundation for longer-term barrier-island evolution and habitat, and Section 5 summarizes our conclusions.

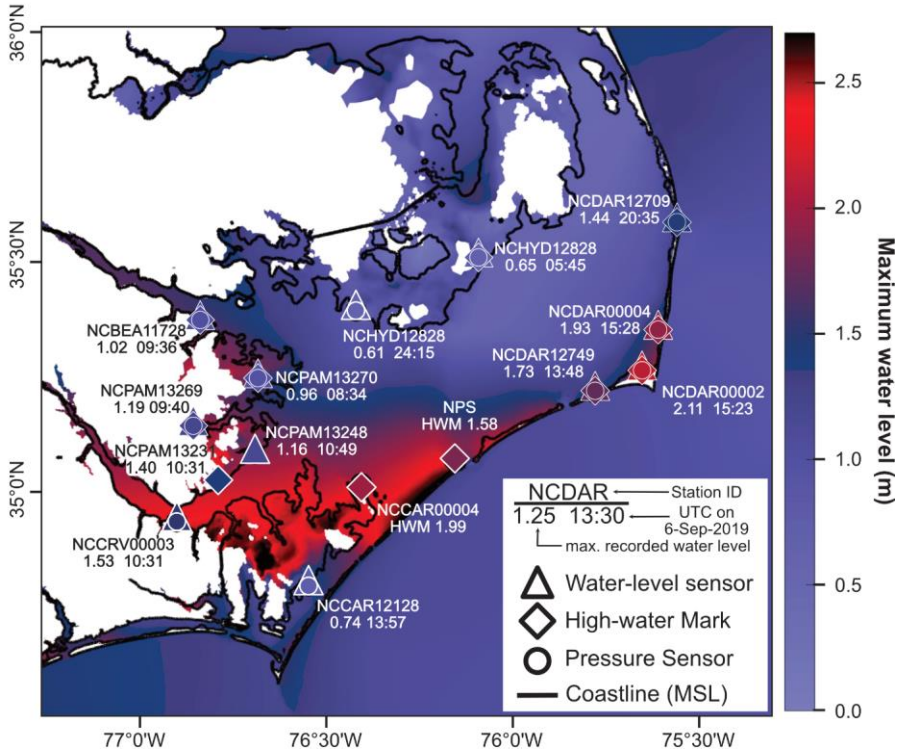

Figure 3. Map of maximum water levels during Hurricane Dorian from measured observations and ADCIRC model forecasts, relative to the North American Vertical Datum of 1988 (NAVD88). Water-levels measured with sensors (circles and triangles) and post-storm high-water marks (HWM; diamonds) in Pamlico Sound; modeled maxima from the ADCIRC simulations (shading). Sources: water levels and high-water mark (HWM) from USGS Flood Event Viewer (https://stn.wim.usgs.gov/FEV/#2019HurricaneDorian); HWM from NPS (H. Crawford, NPS, written comm., August 2022). ADCIRC model forecasts from DHS Coastal Resilience Center at the University of North Carolina, Chapel Hill (adcircprediction.org)

2 Observations and Methods

Observations of the changes wrought by Hurricane Dorian on North Core Banks were primarily derived from remote sensing. The island was evacuated prior to the storm, and access in the year following the storm was curtailed by COVID-19 travel restrictions. As a result, the data we present here are based on aerial imagery, lidar, and peripheral observations, rather than in situ measurements. The remote-sensing data (Table 1) include five sets of high-resolution red-green-blue (RGB) aerial imagery suitable for structure-from-motion (SfM) photogrammetry acquired by the U.S. Geological Survey (USGS), RGB imagery acquired during a National Oceanic Administration National Geodetic Survey

(NOAA NGS) Emergency Response Imagery (ERI) flight, and topographic and bathymetric (topo/bathy) lidar data collected by the U.S. Army Corps of Engineers (USACE). Other sources of data include forecasts from the ADvanced CIRCulation (ADCIRC) ocean model and the Simulating WAves Nearshore (SWAN) wave model provided by the U.S. Department of Homeland Security Coastal Resilience Center at the University of North Carolina, Chapel Hill; wave data from the Diamond Shoals National Data Buoy Center (NDBC 41025) buoy; meteorological measurements from the NOAA National Weather Service at U.S. Coast Guard Station Hatteras (Station ID 8654467); water levels and high-water marks around Pamlico Sound from the USGS Flood Event Viewer (https://stn.wim.usgs.gov/FEV/#2019HurricaneDorian); and high-water marks measured in the historical village of Portsmouth by the National Park Service (NPS; H. Crawford, NPS, written comm., August 2022).

2.1 Aerial image collection and photogrammetry products

Images were collected over North Core Banks by C.W. Wright Consulting for the USGS during five missions: one in October 2018, and four in late summer and autumn of 2019 (Table 1). A Sony A7R 36.2-megapixel digital camera was used to capture RGB images once per second from a light plane flying ~60 m s^{-1} at an altitude of ~300 m above ground level. Four approximately shore-parallel flight lines were flown in each mission, from the Virginia-North Carolina border to Cape Fear (October 2018) or to Cape Lookout (all other missions; Figure 1d). Camera locations for the images were determined by recording shutter events with an estimated accuracy of <5 cm (horizontal) and <10 cm (vertical) using data from a dual-frequency (L1/L2) global navigation satellite system. Locations were determined with post-processed kinematic methods using multiple continuously operated reference stations from the North Carolina network. The images have a ground-sampling distance of ~6 cm per pixel and overlap by ~60% in both along-track and cross-track directions. Approximately 2,000-4,000 images of North Core Banks were obtained during each mission. These were initially stored in raw (Sony .ARW) format, but were converted to Joint Photographic Experts Group (.JPEG) format before photogrammetric process using Adobe Camera Raw (version 12.2.1) with quality setting 12 (maximum), the "Camera Neutral" color profile, and no other modifications. Imagery and positional data

Table 1. Remote sensing data sources for imagery, topographic and bathymetric (topo/bathy) lidar, and red-green-blue (RGB) imagery suitable for structure-from-motion (SfM) photogrammetry.

Acquisition Date(s)	Data type	Location	Reference
2-15 October 2018 (2-4 weeks post-Florence; ~11 months pre-Dorian)	USACE topo/bathy lidar	NC	https://www.fisheries.noaa.gov/inport/item/57345
6-10 October 2018 (~3 weeks post-Florence, ~11 months pre-Dorian)	USGS RGB SfM imagery	NC	Images: https://doi.org/10.5066/P91KB9SF Products: https://doi.org/10.5066/P9CA3D8P
30 August and 2 September 2019 (~4-6 days pre-Dorian)	USGS RGB SfM imagery	Outer Banks	Images: https://doi.org/10.5066/P9WR0VB1 Products: https://doi.org/10.5066/P9K3TWY7
7 September 2019 (~1 day post-Dorian)	NOAA/NGS/ERI RGB imagery	East Coast	https://storms.ngs.noaa.gov/storms/dorian/index.html
8, 12-13 September 2019 (~2-7 days post-Dorian)	USGS RGB SfM imagery	Outer Banks	Images: https://doi.org/10.5066/P9TPKMBB Products: https://doi.org/10.5066/P9K3TWY7
11 October 2019 (35 days post-Dorian)	USGS RGB SfM imagery	Outer Banks	Images: https://doi.org/10.5066/P9RRSMOJ Products: https://doi.org/10.5066/P9K3TWY7
11 October 2019 (35 days post-Dorian)	USACE topo/bathy lidar	NC	https://www.fisheries.noaa.gov/inport/item/60197
26 November 2019 (81 days post-Dorian; 10 days post-Nor'Easter)	USGS RGB SfM imagery	Outer Banks	Images: https://doi.org/10.5066/P99TL46N Products: https://doi.org/10.5066/P9K3TWY7

from each flight are available from Kranenburg et al. (2020, 2021a, 2021b, 2022a, and 2022b).

The imagery was processed to derive geolocated digital surface models (DSMs) and orthomosaics using Agisoft Metashape Professional (v. 1.6.5) with a four-dimensional

structure-from-motion (4D SfM) workflow in which images from multiple missions were aligned together (Warrick et al., 2017; Sherwood et al., 2018; Over et al., 2021b). A single ground control point (GCP #34; Brown et al., 2021) was used to constrain the alignment in two 4D SfM groups. One group contained images from the 2018 post-Florence survey, the August 2019 pre-Dorian survey, and the September 2019 post-Dorian survey. The second 4D SfM group included the October and November 2019 surveys. Following the initial alignment, weak tie points were removed, and the camera calibration and camera locations were adjusted before the creation of dense point clouds and 1-m non-interpolated DSMs in a process described in detail by Over et al. (2021b), based on the work of Breithaupt et al. (2004), Thoeni et al. (2014), Matthews, Noble, and Breithaupt (2016), T. Noble, TN Photogrammetry, oral communication (2016), and Warrick et al. (2017). The median signed difference between 34 GCPs collected between Oregon Inlet and Hatteras Inlet (Brown et al., 2021) and DSMs (GCP - DSM) across all flights for a given 4D reconstruction was used to adjust each DSM in gdal_translate (Geospatial Data Abstraction Library; https://gdal.org/). For the pre- and post-Dorian DSMs, this value was -0.029 m; for the October and November DSMs, it was -0.034 m. The adjusted DSMs were masked using a hand-edited shapefile that aimed to exclude data with a standard error greater than 0.013 (the elevation standard deviation divided by the square root of the sample size), usually caused by water. Orthomosaics with 0.25-m resolution were constructed in Metashape from interpolated DSMs by RGB-averaging overlapping images. Horizontal coordinates are in NAD83(2011) Zone 18N meters, and vertical coordinates (and all elevations in this paper) are in meters NAVD88 using geoid 12B. Examples of the 30 August 2019 (pre-Dorian) and 12-13 September (post-Dorian) orthomosaics are shown in Figure 4, along with the post-Dorian DSM and a difference map (post- minus pre-). The photogrammetry products are available from Ritchie et al. (2022).

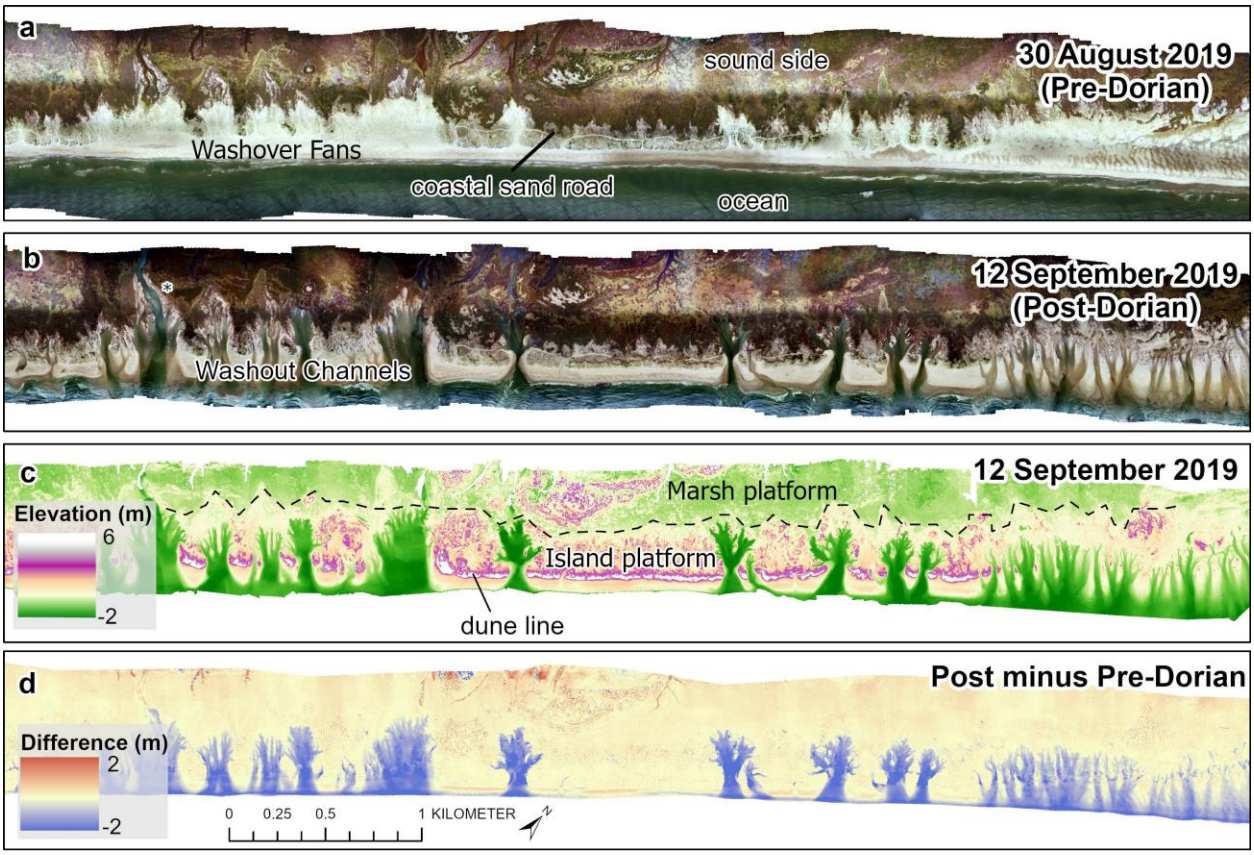

Figure 4. Structure-from-motion (SfM) photogrammetry products. Orthomosaics from a) pre-Dorian survey and b) post-Dorian survey, c) digital surface model (DSM) from the post-Dorian survey, and d) difference map (post-Dorian minus pre-Dorian), where blue indicates erosion. Extensive washover from Hurricane Florence (2018) is visible in (a). Washout channels (b, c, and d) eroded up to 2 m and occupy much of the washover fans. Location of a cross-island channel is marked with an asterisk (*) in (b). Location of these maps is outlined as dashed box in Figure 1b. The sound side is at the top and the ocean is at the bottom of each panel.

2.2 Missing data and uncertainties in the DSMs

The SfM photogrammetry did not provide complete, continuous coverage. Variations in coverage were caused by variations in the flight lines, changing water levels, and shoreline change on the ocean side. Internal data gaps occurred where SfM reconstruction failed, either because of water or restricted view angles near steep objects, usually tall vegetation. In the vegetation cases, only scattered and mostly isolated pixels were missing. These small regions (≤5 m square) of missing data were replaced by values derived from smoothed, interpolated surfaces calculated by convolving a 5 m x 5 m Gaussian kernel over the DSMs.

The larger regions of missing data posed a more consequential problem. Because most of the flooded regions and thus most of the missing data occurred in eroded portions of the post-Dorian DSMs, ignoring these regions in volume-difference calculations would bias the results, generally underestimating erosion. The water levels in the eroded regions varied among the four surveys, as indicated by the mean of the lowest elevations mapped on the ocean beaches. Those elevations were 0.11 m, 0.11 m, 0.64 m, and -0.14 m for the August, September, October, and November surveys, respectively, indicating that ocean-side water levels (driven by tides, surge, and wave runup) were comparable for the pre- and immediate post-Dorian surveys, higher for the October survey, and lower for the final November survey. Thus, many of the erosional areas in the post-Dorian September DSM were flooded. Likewise, these areas and some of the areas where post-storm accretion occurred between September and October were flooded in the October survey. Low water levels during the November survey revealed both deeper portions of the eroded areas and recently accreted sandbars, spits, berms, and washover deltas.

We used several methods for treating the missing data. The first, and simplest, method was to ignore missing data in volume and volume-change calculations; this is equivalent to assuming zero change when elevations in either map are missing. Other methods were to replace missing elevation data with a constant value intended to reflect the average elevation of flooded regions. We calculated volumes and volume changes after replacing missing elevations with 0 m, -1 m, and -2 m. We also used two interpolation schemes to replace missing values using nearby values, including interpolation based on a 30 x 30 m Gaussian kernel, and interpolation based on empirical Bayesian kriging (EBK). The first four methods provided a time series of four surfaces with no gaps, and the interpolation methods resulted in surfaces with small regions of missing data in some of the larger eroded areas. The analyses presented here was based on the EBK surface, but the differences that arise in volume-change calculations using other methods are discussed.

2.3 Uncertainty in digital surface models and volume-change calculations

Uncertainties in our calculations of volume change for a given set of DSMs (e.g., the EBK surfaces) were estimated using the approach described in Anderson and Pitlick (2014)

and Gaeuman et al. (2017) and summarized by Anderson (2019). Three general types of error can arise in elevation difference maps: uncorrelated random errors (imprecision), spatially correlated random errors (regional biases), and systematic errors (global biases).

Uncorrelated random error in difference of DSM (DoD) maps mostly arise from random vertical errors in each independent measurement or small-scale (order ~1 m) variations in topography or vegetation that are aliased in the measurement process. Horizontal errors are less important in low-slope environments like North Core Banks. The uncorrelated random spatial uncertainty σ_{rs} is represented by the standard error $\sigma_{rs} = \sigma_{rmsd}/\sqrt{n}$, where σ_{rmsd} is the root mean square deviation in difference measurements and n is the number of cells in the DSMs (Lane et al., 2003; Anderson and Pitlick, 2014). σ_{rmsd} is the quadrature sum of σ_{rms}, the root-mean square errors in each of the two maps being differenced (Taylor, 1997; Lane et al., 2003). We cannot estimate σ_{rms} in our North Core Banks maps because we have no ground-truth measurements to compare with, but even if we stipulate a large uncertainty in individual measurements (for example, 0.3 m), because n is ~10 million, random errors largely cancel when averaged over the mapped study area. Consequently, our volume calculations are almost completely insensitive to this uncertainty, consistent with discussion by Anderson (2019).

Uncertainty σ_{sc} that arises from spatially correlated errors is a greater source of error than random errors in both DSMs and difference maps. In SfM-derived surfaces, these errors appear as low-amplitude modulations over tens to hundreds of meters in the reconstructed surface, or as apparent vertical offsets with spatial scales equal to the footprint of one or several images. It is often hard to pinpoint the source of these errors, but they likely are related to misalignment in the geometric reconstruction of camera locations or errors in the lens models. The errors tend to track flight paths, suggesting they are related to (or exacerbated by) the intersection of view angles. Quantifying the spatial correlation associated with these errors is necessary for determining the effective number of random samples in each map area. Following Rolstad et al. (2009), we used semivariograms to estimate the spatially correlated errors σ_{sc} (m) and their characteristic length scales r (m). The expected error variance σ_{sc}^2 is equivalent to the semivariance γ^2 and acts as systematic error over an area proportional to πr^2 (m^2), where r (m) is the

range of the semivariogram. We determined $\sigma_{sc}^2 \approx 0.03$ m^2 and $r \approx 36$ m from the mean of sills and ranges fit to spherical semivariogram models of elevation differences in 22 subregions of our survey area where there was limited morphologic change (Rolstad et al., 2009).

Systematic errors (biases) are likely to contribute the greatest errors in difference calculations. They can be determined empirically when parts of the mapped area are known to be stable (e.g., Rolstad et al., 2009; Anderson, 2019) but there are few, if any, truly stable features on North Core Banks and no large, unvegetated areas that are not subject to reshaping by wind or water. To compare maps, we assumed that cabin roofs, the ferry dock at Long Point, and high-elevation unvegetated patches were stable features for calculating systematic uncertainties. We identified elevations z of 50 points distributed around the island and calculated the four-survey mean elevation $\bar{z}$ of each. We then calculated the anomalies $dz = z - \bar{z}$ for each of the 50 points. The mean anomalies $\overline{dz}$ for the four surveys ranged from -2.4 cm to +2.2 cm. These values were used to vertically shift each DSM as described in the previous section so that, on average, there was no elevation difference among the final DSMs for nominally stable points. That is, the measurable systematic bias among the surveys was removed. However, we cannot be certain that no systematic bias remained, because of the limited spatial extent of the data analyzed, so we used the maximum of the standard deviations of the anomalies (0.07 m) as an estimate of systematic uncertainty σ_{sys} (Rolstad et al., 2009; Anderson, 2019). This value dominates our estimates of uncertainty in volume calculations as noted below.

The total uncertainty surrounding the volume calculations is approximated as the quadrature sum of the random, spatially correlated, and systematic errors (Anderson, 2019, his Eq. 22):

$$\sigma_v = nL^2\left(\sigma_{rs}^2 + \sigma_{sc}^2 + \sigma_{sys}^2\right)^{\frac{1}{2}} = nL^2\sigma_{tot} \quad (1)$$

where n is number of grid points (>10 million for the entire island) and L^2 = 1 m^2 is the grid cell size. The terms in the brackets represent uncorrelated random errors, spatially correlated errors, and systematic errors, respectively. Values for the three terms in the brackets of Eq. 1 are $\sigma_{rs} = 6{\cdot}10^{-5}$ m, σ_{sc}= 0.035 m, and σ_{sys}=0.07 m, which results in a σ_{tot}

438 value of 0.08 m. This suggests that the total uncertainty (0.08 m) is dominated by the
439 conservative estimate of systematic uncertainty (0.07 m).

440 2.4 Wrack deposits

441 Wrack deposits of marsh hay were clearly visible in the post-Dorian imagery,
442 scattered broadly across the marshy portions of the back barrier and concentrated in
443 clumps ~0.5 to 1 m thick on the back (landward) side of the primary dunes. Wrack
444 stranded against the dunes can indicate water elevations at the peak of the inundation (e.g.,
445 Bush et al., 1996; Clinch et al., 2012). We identified wrack deposits in the post-Dorian
446 orthomosaic based on their color and shape and extracted the elevation of the wrack toe
447 (lower, landward edge) from the 1-m DSM at ~11,000 points spaced 1-m apart (Figure 5).

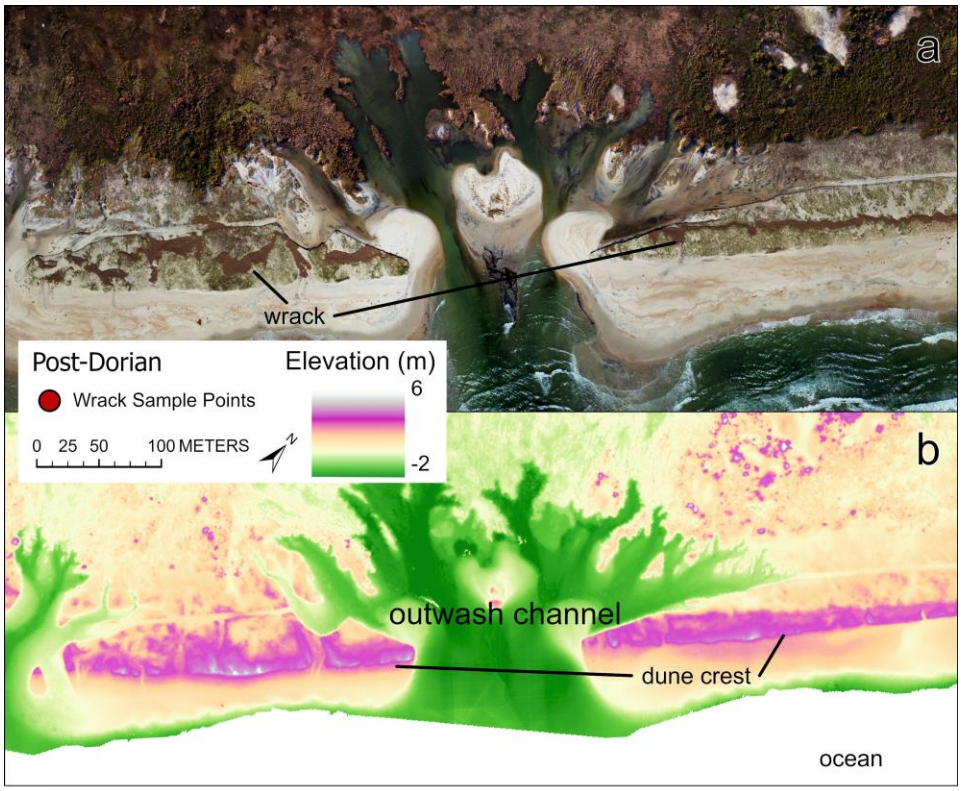

448

449 **Figure 5. Example of wrack stranded on the landward side of the primary dune line.**
450 **a) Orthomosaic showing large piles of brown wrack on the northwest flank of the**
451 **dunes. b) Outlines of wrack deposits overlain on DSM adjacent to the orthomosaic.**
452 **Points sampled to establish the toe elevations of the wrack deposits are shown on**
453 **the DSM. Location of these images is indicated by the small orange box in Figure 1b.**

454

455 2.5 Dune-crest elevations and island volumes

456 The elevations of the primary dune lines were extracted from the four 1-m SfM EBK
457 DSMs after a) manual clipping to remove ocean-side bars (isolated patches seaward of the
458 beach surrounded by missing data) and b) remapping them (nearest-neighbor
459 interpolation) into 1-m grids with axes oriented alongshore (42^0 clockwise from UTM grid
460 north) and cross-shore (222^0). Remapping into alongshore and cross-shore coordinates
461 allowed us to analyze the data as a series of two-dimensional cross-shore transects spaced
462 1 m apart, which facilitated automatic identification features such as the shoreline and
463 dune crest. Finally, c) the elevations of each DSM were adjusted vertically to account for
464 cm-scale mean vertical biases discussed above. Bias corrections were -0.022 m, 0.002 m,
465 0.005 m, and 0.015 m for August (pre-Dorian), September (post-Dorian), October, and
466 November DSMs, respectively. The dune crest was demarcated by the highest point on each
467 cross-shore transect within 30 m of an approximate dune line manually digitized on the
468 August DSM, guided by elevation, with straight-line connections across gaps. Elevations for
469 subsequent surveys were extracted from the locations of the pre-Dorian dune crests.
470 Alongshore profiles of dune-crest elevations after Hurricane Dorian were substantially-
471 lower in many places, as discussed below (Figure 6).

472 Volume calculations were performed for two portions of the island: the beach and a
473 region we call the island platform. The beach was defined as the area between the primary
474 dune crest line interpreted from pre-Dorian SfM DSM and the seaward-most location of the
475 mean high water (MHW; 0.4-m NAVD88) contour. The island platform was defined as the
476 region between the crest of the primary dune line and a back-barrier boundary defined by
477 the 1.25-m contour in the bare-earth post-Florence lidar DEM. We restricted the landward
478 extent of our analysis to this island platform region for consistent coverage and to avoid
479 poor-quality SfM reconstructions in wet and marshy regions. The 1.25-m contour

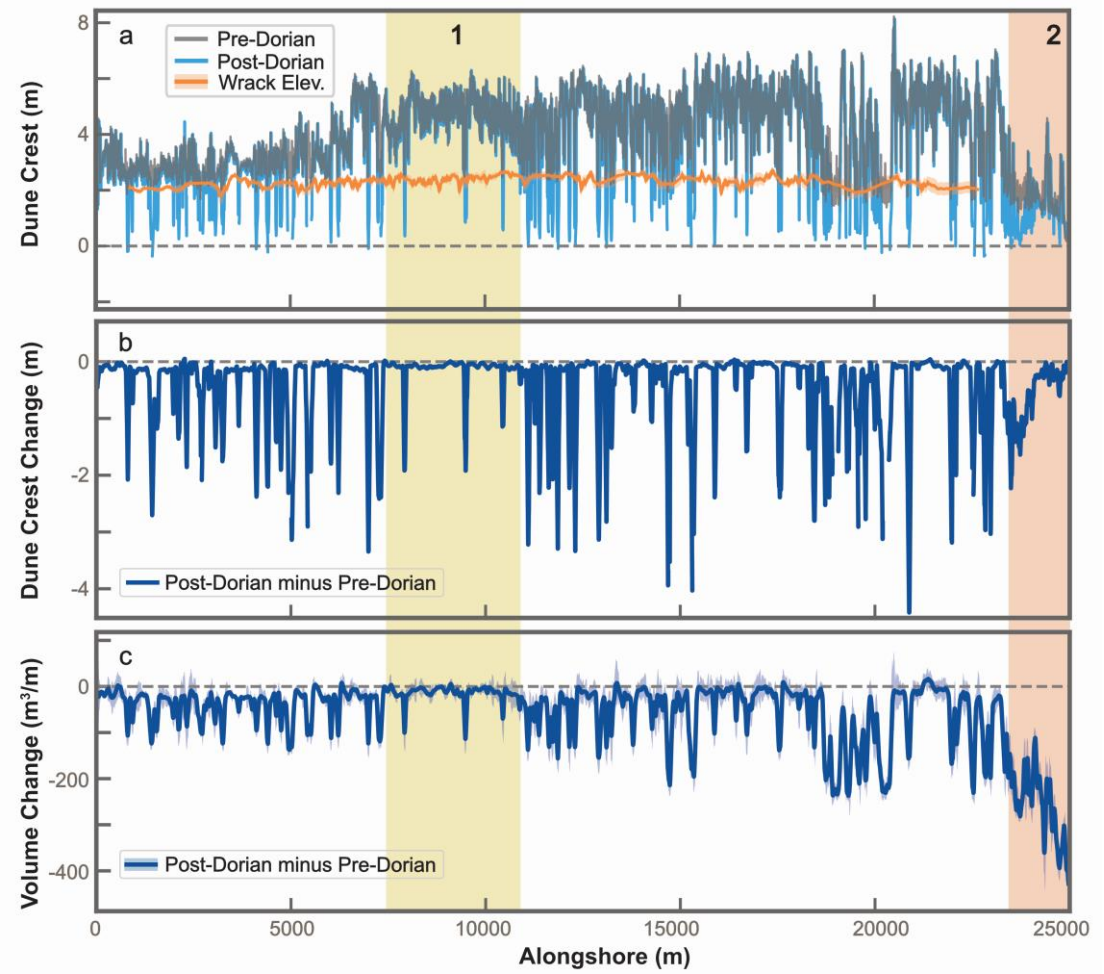

Figure 6. Changes in elevations and volumes. Plots of alongshore values of a) pre-Dorian (gray) and post-Dorian (blue) dune-crest and wrack-line (orange) elevations, b) dune-crest elevation changes, and c) total volume changes. All curves have been smoothed with a 50-m alongshore running mean. Uncertainties around the volume changes are indicated in light blue. Area 1 (beige) highlights a segment of the island with high dune crests and relatively few washouts, and area 2 (pink) highlights a region with initial low dune crests and large volumes of erosion.

roughly tracked the change in vegetation from bushes and scrubby trees on the island platform to grasses and reedy vegetation in the marsh and provided a landward limit for our analysis that was consistent across surveys. The boundaries established by the pre-Dorian primary dune line and the back-barrier limit, and thus the platform areas, were constant across surveys, but the seaward extent, and thus the beach areas, varied across surveys.

Volumes were calculated by summing elevations along each cross-shore transect and multiplying by the cross-shore spacing (1 m) and then summing those transect volumes in the alongshore direction and multiplying by the alongshore spacing (1 m). Volume changes were performed in a similar manner by differencing the volumes on each transect between surveys. The advantage of this transect approach was that it provided information on volume changes along the island (Figure 6).

2.6 Shorelines and shoreline change

Shoreline changes along North Core Banks before and after Hurricane Dorian were determined from the pre- (August) and post-Dorian (September), October, and November DSMs using the Digital Shoreline Analysis System (DSAS; v. 5.0; Himmelstoss et al., 2018). First, an offshore baseline parallel to the barrier island was created and 500-m long cross-shore transects spaced 10-m apart with a smoothing distance of 500 m were cast across the foreshore and dune. Shoreline positions were determined from the MHW (0.4-m contour) on the beach from each DSM, which were naturally discontinuous. DSAS shoreline positions were extracted where the contour line intersected each transect; connecting the points at successive transects created a continuous shoreline. If a contour passed a transect multiple times, the seaward-most point was used. The shorelines were hand edited to remove intersects across outwash channels (e.g., Morton and Miller, 2005). Lastly, the DSAS intersects were put into a pivot table to compare shorelines from the four surveys (e.g. Shoreline Change Mapper available at https://irma.nps.gov/DataStore/Reference/Profile/2254678). Examples of the resulting shorelines are shown in Figure 7a, and shoreline changes at each transect that met the conditions above are shown in Figure 7b-d.

2.7 Characterization of washout features

The drainage features generated by outwash during Hurricane Dorian were individually identified and characterized to explore and compare the shapes and sizes of these features along the island. The primary tool to identify these features was the elevation difference between the pre- and post-Hurricane Dorian DSMs from the USGS flights (August and September 2019; Table 1) calculated in ArcPro v2.8.1 (Esri, 2021). First,

a binary difference map (change vs. no change) was created using a difference threshold of -0.25 m. This value represents about three times the error in the DSMs. Areas of change >0.25 m were converted from binary rasters to polygons and visually compared with the orthomosaics to confirm they were drainage features. The polygons were then cleaned for noise artifacts in the DSMs, and shapes that were less than 5 m^2 or in the marsh platform of the island were removed using a combination of area thresholding and manual inspection. Washout features were then clipped at the pre- Dorian dune toe to create standalone polygons, but in some cases where washout features had individual throats and minimal connectivity (i.e., shared a small portion of area in the head-cutting portion of the washout feature) they were split into separate features by comparing with the post-Dorian orthomosaics. A continuous stretch of washout channels present at the northern end of North Core Banks was not included in this analysis because no dune line existed there before Hurricane Dorian, and the difference threshold did not resolve individual features in this area.

This analysis identified 86 individual washout channels on North Core Banks. The planview shapes of the drainage features associated with the channels were classified according to a system modified after Hudock et al. (2014) to describe washover feature shapes. We renamed Hudock's "dissipative" class with the more morphologically descriptive term "tapering" to prevent confusion with physical processes. Examples are shown in Figure 8. Visual inspection indicated that washout drainages tended to occupy the same locations as earlier washover fans (Figure 4). Fresh-looking washover fans were apparent in the November 2018 (post-Florence) orthomosaic (Ritchie et al., 2021) i.e., they were unvegetated and sometimes showed flow features like current lineations, in contrast to the surrounding washover platform, which was modestly vegetated and showed evidence of aeolian reworking in the form of small dunes and blowouts. The

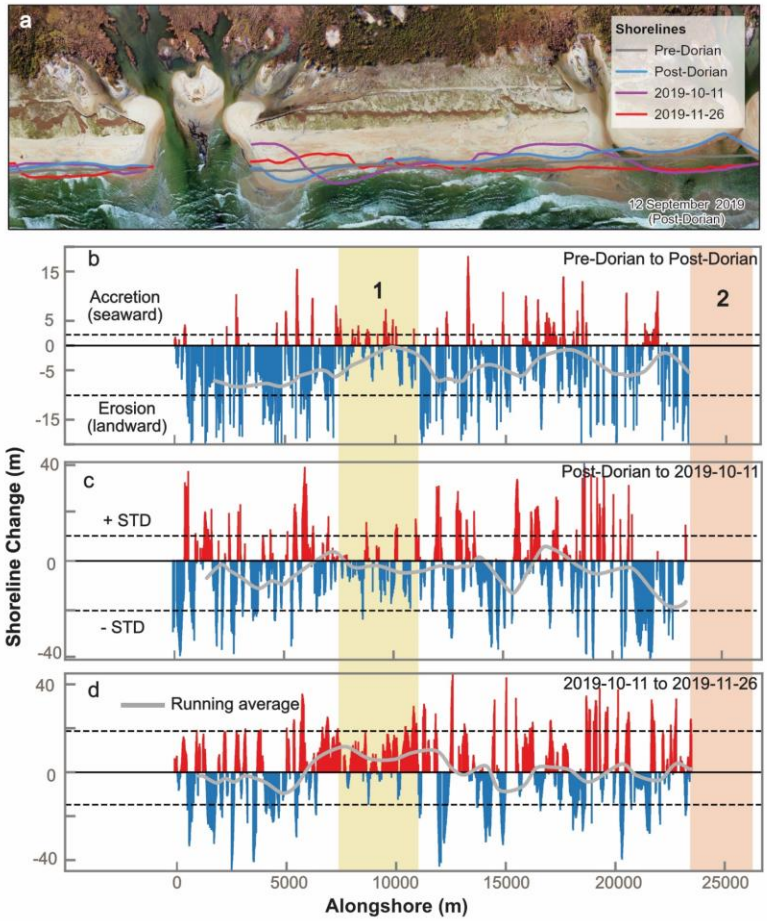

Figure 7. Shoreline-change analysis, note different y-axes. a) Shoreline positions and locations of transects for an exemplar 1.5-km stretch of coast post-Dorian, b-d) Spatially averaged changes in shoreline positions between survey dates for the entire North Core Banks. Each vertical bar is the shoreline position change every 10 meters along the beach, except at washout channels, between two dates and the gray line represents a running average. One standard deviation (STD) is also given as dashed black lines. The beige and pink bars highlight areas that deviate from the general trend; area 1 is near the center of the island where fewer washout channels formed and area 2 is at the northeast end of the island, where the most severe erosion occurred (see Figures 4, 6), and where it was difficult to identify shorelines.

Florence washover fans sloped landward continuously from the beach through gaps in the dune line and buried the shore-parallel sand road behind the foredune. At their distal ends, tendrils of sand deposits covered pre-existing vegetation. They are still mostly visible in the August 2019 (pre-Dorian) orthomosaic (Figure 4) but are somewhat more vegetated and less distinct. The footprints of these fans were identified in the post-Florence orthomosaic using a supervised classification in ArcPro v2.8.1 (Esri, 2021). A workflow like the one

described above for washout features was used to remove noise and the polygons were clipped to the pre-Dorian dune toe.

Allometry metrics (Bull, 1975; Lazarus, 2016; Lazarus et al., 2020) were extracted for each post-Dorian washout drainage and each post-Florence washover feature, including minimum area envelope A, volume V (Figure 8b), maximum intrusion length L, maximum drainage width W, throat width T, average throat depth D (post-Dorian only), perimeter P, and enclosing convex hull area A_c (e.g., Lazarus et al. 2020; their Table 2). We examined the relationship between A and L by fitting $\log_{10} L = h \log_{10} A$, where h defines the slope of the relationship in a log-log transform space (Figure 8c; Lazarus, 2016; Lazarus et al., 2020). We also examined the log-log relationship between A and V (Figure 8d) which Lazarus et al. (2022) have used to relate washover areas and volumes. Finally, we calculated several morphometric indices to evaluate the apparent similarities in the shapes of outwash and overwash features. These included the circularity ratio $C_r = 4\pi A/P^2$ (Jones et al., 2012; Das et al., 2022, their eqn. 12), which is the ratio of feature area to the area of a circle with the same perimeter; a second, somewhat related ratio $R_2 = A/A_c$, where A_c is the area of the convex hull enclosing the feature area; the distortion index $DI = P/[(\pi+2)(2A/\pi)^{0.5}$ proposed by Lazarus et al. (2021; their eqn. 1 and 2), which is the ratio of the measured perimeter of a feature to the perimeter of a semicircle with the same area; and the indenture index $I = 0.5PL/(A+L^2)$ (Das et al., 2020, their eqn. 25), which relates the measured perimeter to the perimeter of a rectangle with the same A and same L. All these indices indicate the complexity of the boundary of a given area and displayed similar abilities to discriminate among the various shapes, so we chose to use DI (Figure 8e) because it relates to a common depositional fan shape (Lazarus et al., 2021 and citations therein).

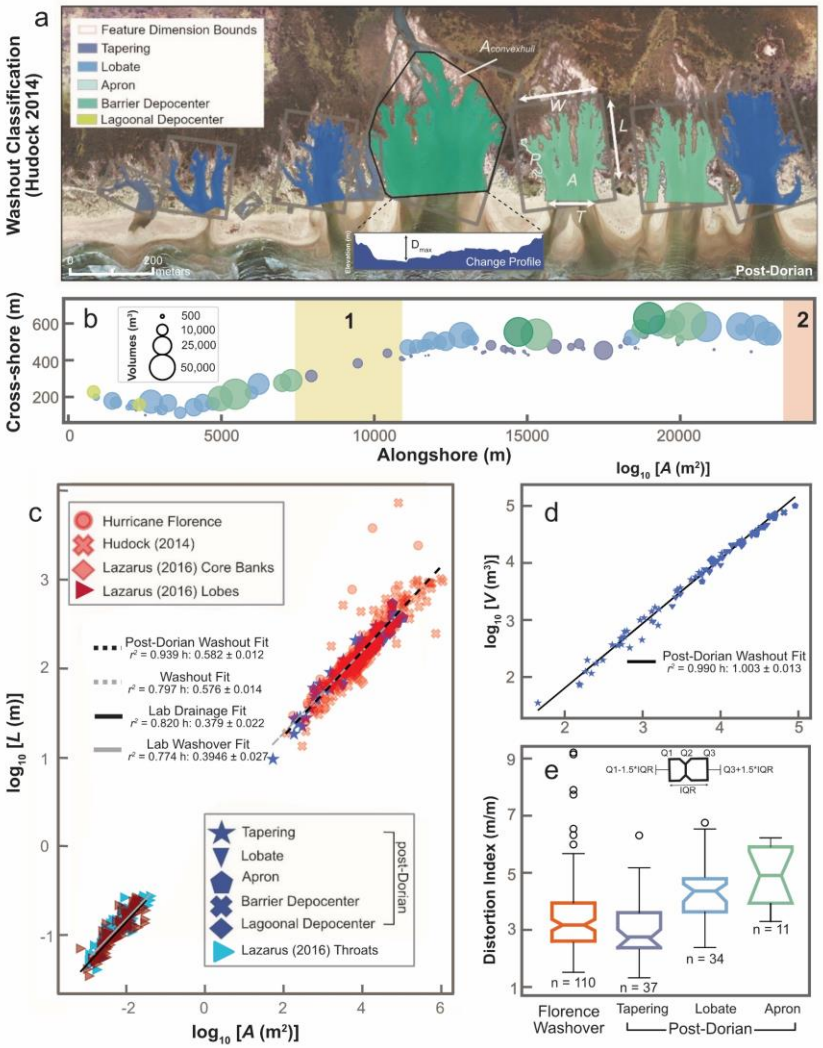

589

590 **Figure 8. Allometry of erosion features visible in post-Hurricane Dorian DSM and**
591 **orthomosaics. a) Illustration of washout-feature classification by shape and**
592 **examples of how metrics were derived. Areas 1 and 2 as on Figures 4, 6 and 7. b)**
593 **Volumes of washout features with colors indicating shape classes, plotted at their**
594 **alongshore and cross-shore centroids. c) Scatter plot of feature length L versus area**
595 **A in log-log coordinates, with symbols indicating the data source. Depositional**
596 **features (overwash fans, lobes) are red, and erosional features (outwash, throats)**
597 **are blue. Linear fits to the North Core Banks outwash (black dashed line) and several**
598 **overwash datasets (gray dashed line) are shown for the real-world features. Fits to**
599 **the Lazarus (2016) laboratory data for throats (black solid line) and lobes (gray**
600 **solid line) are also shown. Panel (d) is a scatter plot of feature volume V change**
601 **versus A in log-log coordinates with symbols the same as in (c). Panel (e) has box**
602 **plots of the Distortion Index distributions. In these plots (matplotlib.pyplot.boxplot,**
603 **v.3.5.3), the box indicates the interquartile range (IQR), the whiskers extend to 1.5 x**
604 **IQR, beyond which outliers are denoted with circles. The notches indicate bootstrap**
605 **estimates of the confidence intervals about the median values.**

606 # 3 Results

607 ## 3.1 Water levels and waves during Hurricane Dorian

608 Forecasts made with the ADCIRC hydrodynamic model during Hurricane Dorian
609 show the evolution of water levels across North Core Banks. During the early part of the
610 event before landfall, the model showed slight increases in ocean-side water elevations and
611 increasing set-down of water levels in the south side of Pamlico Sound, as easterly winds
612 pushed water to the northeast portion of Pamlico Sound (Figure 2). After landfall (approx.
613 1200 Coordinated Universal Time (UTC) on September 6, 2019; Figure 2), as winds veered
614 rapidly to blow from the north-northwest, simulations show the water was forced
615 southward across Pamlico Sound, possibly aided by seiching, and generated water levels >2
616 m on the sound side of North Core Banks. By about 1300 UTC on 6 September, offshore
617 winds gusting >60 m/s caused set-down on the ocean side, creating water-level differences
618 of >2.5 m between Pamlico Sound and the ocean. (We note that simulations by Cassalho et
619 al., 2021 using the same models but different wind forcing produced lower maximum water
620 levels). High-water marks were recorded at almost 2 m NAVD88 on Cedar Island on the far
621 side of Core Sound, about 15 km west of North Core Banks, and the highest modeled water
622 elevations, found along the sound side of the North Core Banks, were over 2.5 m (Figure 3),
623 in agreement with the ADCIRC forecasts. Several cows pastured on Cedar Island were later
624 found alive on North Core Banks after being swept across Core Sound
625 (https://www.washingtonpost.com/nation/2019/11/14/cedar-island-cows-hurricane-
626 dorian-outer-banks/, last visited 5 April 2021). Their journey is the subject of a story by
627 MacKinnon (2023) that provides a feel for conditions during the storm. High water marks
628 ranging from about 1.9 to 2.2 m NAVD88 were recorded by the NPS in the abandoned
629 village of Portsmouth on the north end of North Core Banks (H. Crawford, NPS, written
630 comm., August 2022). These water levels exceeded the average elevation (~1.5 m) of North
631 Core Banks and the elevations of low points and gaps in the island's dune crest (~ 2.0 m),
632 indicating that the island was inundated from the sound and water-level differences across
633 the island approached 2.5 m.

Coincident with these water-level differences, the ocean waves measured at the Diamond Shoals buoy (NDBC 41025) peaked with significant wave heights of ~8.1 m and dominant periods 10.8 s at 1140 UTC (Figure 2), but their impact on North Core Banks was likely mitigated by low ocean-side water levels. By the next high tide (~1800 UTC), wave heights had decreased to about 4.3 m, with periods of 9 s. Wave direction was not measured by the buoy.

3.2 Landcover and morphology changes

The pre-hurricane topographic and orthomosaic data from August 2019 portray the low-lying barrier island with mean and maximum elevations of 1.5 m and ~8 m, respectively (Figures 4 and 5). The ocean-side beach between the dune crest and MHW (~0.4 m) was ~50 – 70 m wide with a discontinuous berm crest at ~2.1 – 2.3 m. Behind the beach was a discontinuous primary dune rising from a toe elevation of ~1.5 – 2.2 m to crests ranging from 3 to 8 m. Beach berms at an elevation of 2 – 2.5 m occupied gaps in the dune lines. Behind the dunes was a plain of coalescing washover fans (e.g., Figure 4a). Many of these fans appear to be recently deposited: they had little or no vegetation and examination of post-hurricane images suggests they were likely deposited during Hurricane Florence (2018). The elevation of the island platform landward of the dunes gradually decreased and the landcover shifted from sparse dune grass to patchy brushy vegetation. The back side of the island was a marsh platform that formed an irregular coastline in Pamlico Sound. Historical records show much of this marsh occupied abandoned flood-tidal deltas associated with ephemeral inlets (Riggs and Ames, 2007).

The first images available after Hurricane Dorian were the NOAA/NGS Emergency Response Imagery taken on 7 September 2019, the day after the storm. (https://storms.ngs.noaa.gov/storms/dorian/index.html; Figure 1b-d). These images revealed an island dissected by more than 80 washout channels cutting through the primary dune line. Landward of these channels, embayments and outwash channels were eroded into the washover plain. These features mostly occupied the same footprint as the recent washover fans. They originated near the distal edge of the recent washover fans, with knickpoints that sometimes extended into the vegetated platform landward of the

663 fans. Many of the embayments were completely or partially flooded. Where they were
664 unflooded, there was abundant evidence of seaward-directed flow in the form of shallow
665 braided channels, sheet-flow deposits, streaks of dark-colored sediment, and lateral
666 channel scarps. Many of these washout features extended from behind the dunes, through
667 recently enlarged cuts in the dune line, and across the upper beach (Figure 1c-d; Figure 4,
668 Figure 5). Cuts in the dune line occupied locations of pre-storm overwash channels and
669 human-made access roads. A shore-parallel sand road behind the primary dune line was
670 cut by the channels and was widened and scoured by erosion. Standing water ponded in
671 low spots behind the dunes. Four channels extended entirely across the island to Pamlico
672 Sound (one is noted with an asterisk in Figures 4b and 11a); these were in the northeast
673 part of the island, at the locations of earlier ephemeral inlets identified by Riggs and Ames
674 (2007).

675 Offshore, irregular seas appeared in the images (Figure 1c, d). In some nearshore
676 regions, swells with wavelengths ranging from 40 to 60 m were present, approaching the
677 shore from ESE. Nearshore, the patterns of breaking waves indicated the presence of
678 shallow wave-dominated deltas where the eroded sand was deposited. Many of the largest
679 of these deltas induced wave breaking >250 m or more offshore, double, or triple the width
680 of the surf zone fronting beaches without channels. Plumes of dark brown suspended
681 sediment were visible, extending more than 500 m offshore. Despite the slight angle of the
682 wave approach to the shoreline, there was no evidence of alongshore flow in the foam or
683 suspended-sediment plumes. Small spits and swash bars had formed, partially closing
684 some of the smaller channels and providing the first evidence of recovery from the storm.
685 These also showed no preferential orientation or evidence of alongshore transport. Taken
686 collectively, the morphology revealed in these images clearly indicates that the island was
687 mostly inundated from the sound side, the floodwaters drained to the ocean through gaps
688 in the dune line, and the eroded material was deposited in the nearshore region to
689 distances of at least 250 m.

690 Orthomosaics, DSMs, and difference calculations derived from the USGS imagery
691 collected a few days later (12-13 September 2019) allowed us to quantify these changes
692 (Figures 4, 5, and 6). Elevation changes exceeded -2 m (Figures 4, 5) in the drainages. The

elevation changes along the dune crest (Figure 6) indicated that channels formed in gaps where the pre-Dorian elevation was less than about 2 – 2.5 m; this is consistent with the elevation of the wrack line. Wrack was stranded on the back side of the primary dune line at elevations between 1.2 and 3.0 m, with a mean ± std. dev. of 2.3 ± 0.23 m (Figure 5). The elevation of the strand line was a little higher near the center of the island (Figure 6). The elevation distribution along the dune crest was bimodal before Dorian, reflecting a combination of intact dunes, with a modal peak at about 5 m, and gaps in the dune line, with a modal peak of about 2.7 m (Figure 9a). After Dorian, the elevation distribution became tri-modal, with substantial reduction in the 2.7-m mode and a new mode at ~0.7 m. This signifies erosion as channels incised vertically in the gaps and laterally into the adjacent high dunes.

The channels had relatively narrow throats (median 52 m; see Table 3 for statistics of all channel parameters) where they crossed the primary dune line but, landward of the dunes, they expanded into dendritic drainage basins up to >300-m wide that mostly occupied the recent washover fans (Figures 4, 5). These drainages typically extended ~170 m inland from the dune line and were incised up to 2.5-m deep into the previous ground surface to elevations near 0 m (Figure 4d and 5b). Dark brown material, presumably mud or peat, was exposed in the thalweg of several channels (not shown). Channel banks were steep and, in many places, close to vertical. Channel bottoms often appeared to be flat, suggesting either hydraulic control associated with a base level at the ocean water elevation during the storm, or geologic control by a layer of less erodible material (e.g., relict marsh muds).

Initial signs of geomorphic recovery were evident in the orthomosaic from a week after Dorian, as spits and swash bars started to fill the channels (Figures 4, 5, 7). In November imagery (Figures 10 and 11), continued recovery was apparent: beaches widened, continuous berms closed many of the inlets to form ponds, and washover fans partially filled the ponds. The sequence of erosion and initial recovery is illustrated in cross-shore profiles along the channel thalweg (Figure 10a-c; transect A-A' in Figure 1d) and across an adjacent dune and beach (Figure 10d-f; transect B-B' in Figure 1c). During Dorian, a large volume of sand was removed from the beach, dunes, and barrier

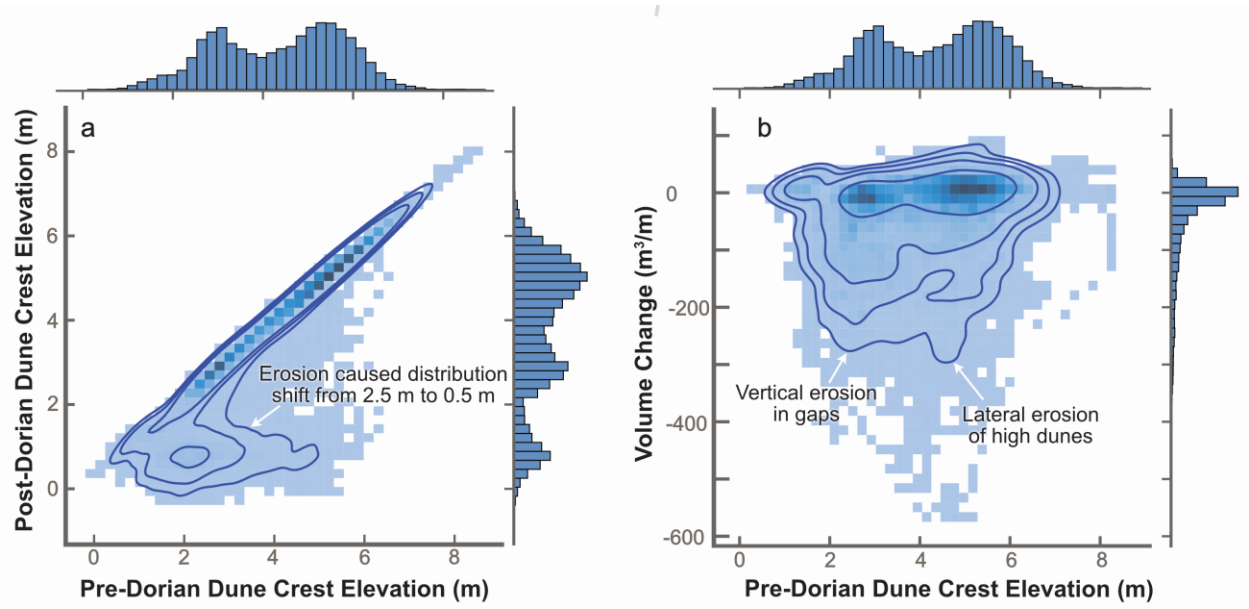

Figure 9. Joint probability plots of the relationship between a) pre-Dorian dune-crest elevation and post-Dorian dune-crest elevation and b) pre-Dorian dune-crest elevation and platform volume change. In both graphs, histograms of the initial elevation distributions appear at the top, and histograms of (a) post-Dorian dune-crest elevation and (b) the volume-change distributions appear on the right, and fractional joint distributions are shaded and contoured in the middle. Darker blue shading indicates more occurrences. Contours levels in (a) are 0.05, 0.1, and 0.2 m; in (b) a 0.5-m contour is added.

platform to form the washout channel (Figure 10a). The dune crest was removed by lateral erosion as the channel widened. Meanwhile, on the cross-dune transect, erosion was limited to the beach (Figure 10d). Between the post-Dorian survey and the October survey, initial recovery took the form of berm building and overwash, partially filling the outwash channel (Figure 10b) and building the beach (Figure 10e). Following a major nor'easter in November, the last survey showed erosion and lowering of the beach and berm, but extensive overwash that deposited sand more than 100 m into the channels and restored some of the initial island volume. The November orthomosaic and DSM (Figure 11) show this widespread overwash filling the channels and berms extending across the channels to form ponds.

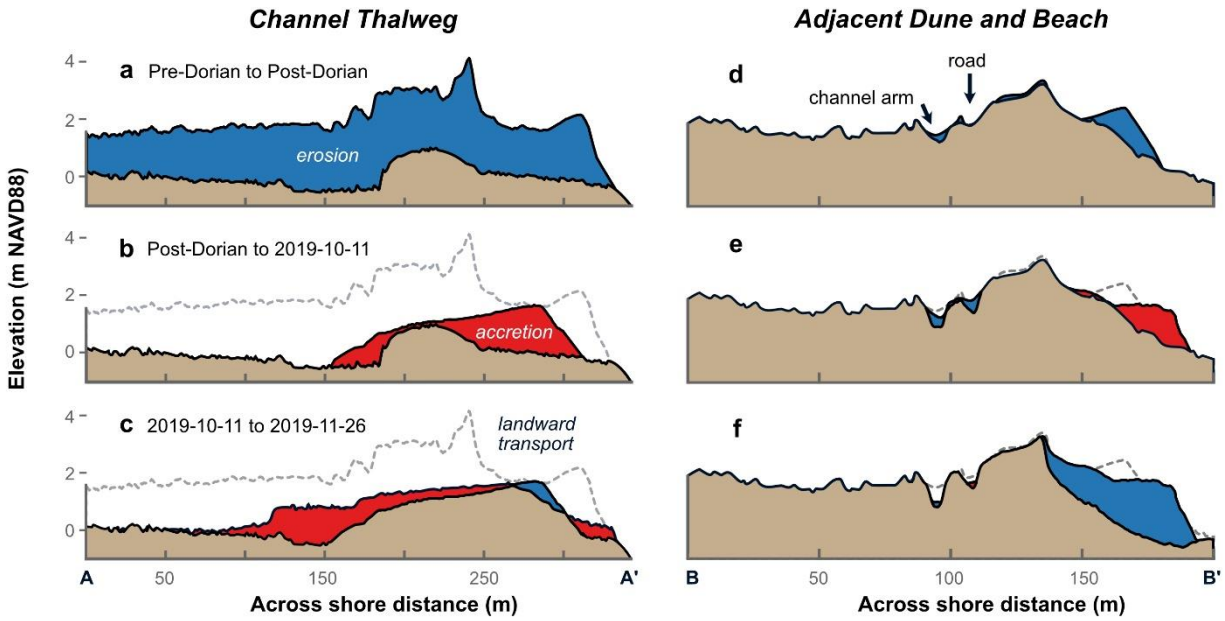

Figure 10. Cross-shore profiles illustrating erosion during Hurricane Dorian and subsequent partial recovery. Panels (a), (b), and (c) show the sequence of profiles along an outwash channel thalweg (transect A – A' in Figure 1) before Hurricane Dorian, after Hurricane Dorian, and in November 2019. Panels (d), (e), and (f) show the sequence of profiles across a dune adjacent to an outwash channel (transect B – B' in Figure 1.)

3.3 Volume changes

Substantial loss of island volume occurred during Hurricane Dorian that was not regained within the three months of our post-storm observations, regardless of the calculation method and uncertainty. The subaerial volume of North Core Banks, defined by the elevation above 0 NAVD88 of the pre-storm (August) EBK DSM for the beach and island platform was found to be 16.6 ± 0.9 Mm^3 (Figure 12). Volume estimates using other methods for filling missing data were not significantly different (Figure 12; Table 2). Erosion during Hurricane Dorian reduced this volume to 13.7 ± 0.9 Mm^3, a reduction of about 18% of the initial volume. The amount of erosion on individual cross-island transects varied greatly, ranging from losses of -440 $m^3\ m^{-1}$ to gains of 12 $m^3\ m^{-1}$ (5^{th} and 95^{th} percentiles) with a mean ± std. deviation

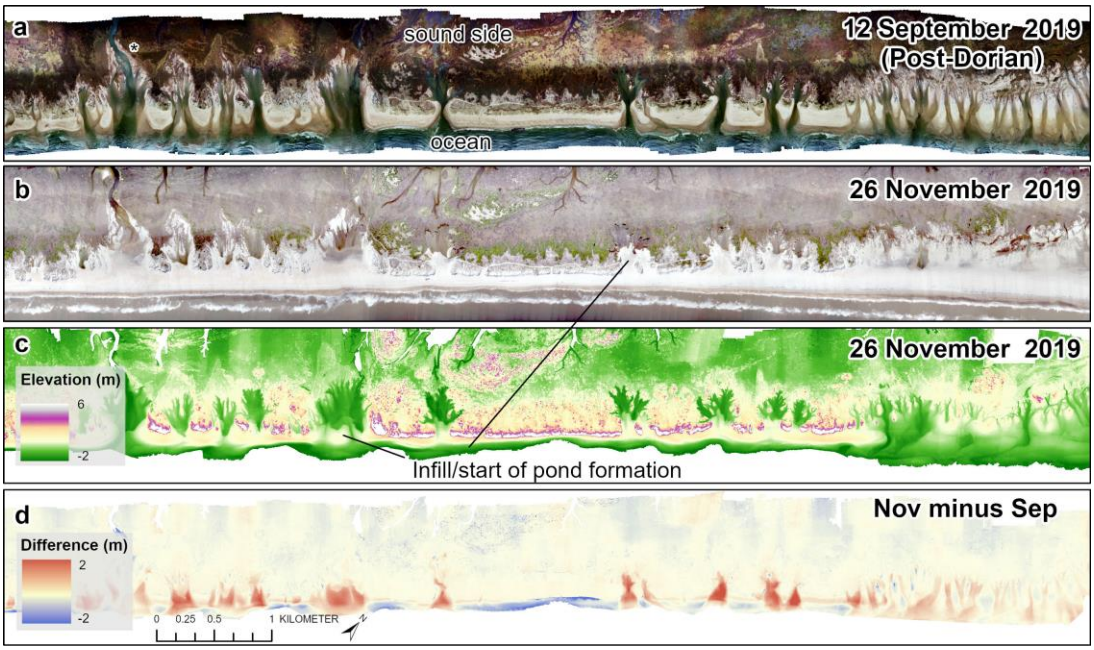

Figure 11. Post-Dorian structure-from-motion (SfM) photogrammetry products. Orthomosaics from a) September post-Dorian survey and b) November survey after a powerful nor'easter. c) Digital surface model (DSM) from November survey. d) Difference map (November minus September post-Dorian); erosion is blue and deposition is red. Location of a cross-island channel is marked with an asterisk (*) in (a). Location of these maps is outlined as dashed box in Figure 1b. The sound side is at the top and the ocean is at the bottom of each panel.

of -117 ± 147 m^3 m^{-1} (Figure 7c). The median uncertainty for these measurements is 74 m^3/m. The high variance in erosion along transects was related to the non-uniform pattern of erosion, which was highest in the outwash channel networks and moderate to negligible elsewhere.

The volume measurements included the influence of vegetation canopy, because the SfM-derived DSMs included vegetation. These DSMs positively biased the measurements of subaerial island volumes, because of the canopy, which was generally highest in the shrubs and small woodlands of the back barrier. However, volume change measurements included lower biases because very little of the volume change occurred in vegetated regions (e.g., Figure 4). The greatest differences in DSMs among surveys were within the drainage features that mostly cut through unvegetated and sparsely vegetated areas of beach, washover platforms, and dunes.

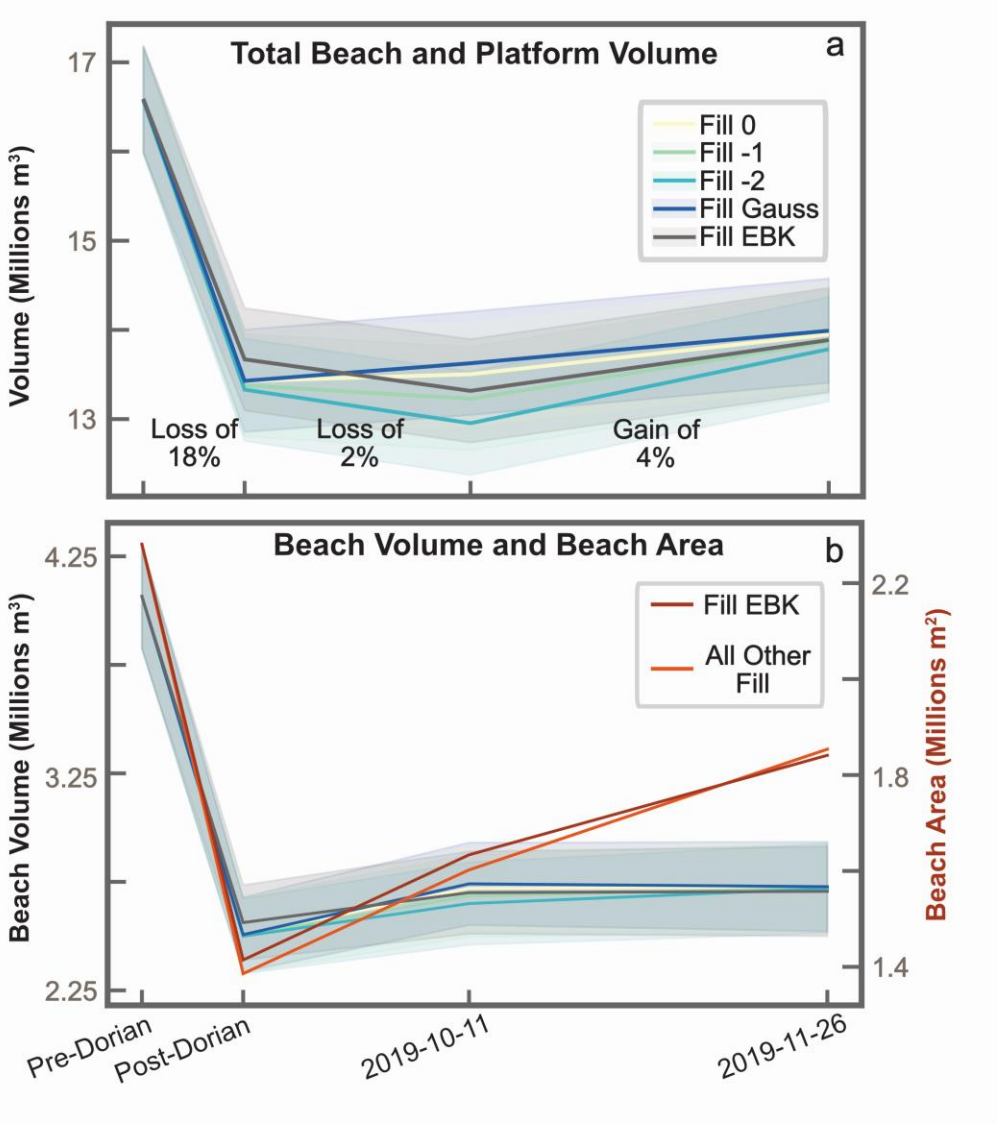

Figure 12. Summary of volumes and beach areas. a) Total volumes of the combined beach and island platform calculated using five different methods of replacing missing data, for each of the four surveys. Fill 0, -1, -2 refer to surfaces where missing data were filled with uniform values of 0, -1, or -2 m. Gauss refers to surfaces filled with interpolation with a Gaussian kernel. EBK refers to surfaces formed using the empirical Bayesian kriging method. b) Volumes of the beach using the same five methods for replacing missing data, for each of the four surveys, overlaid with beach areas, also calculated using the five methods. Shaded bands around the volumes indicate uncertainty (see text).

The distribution of volume losses as a function of initial dune-crest elevation were not confined to places with low initial elevations (Figure 9b) because some high-elevation

dunes were eroded laterally, but the largest loss rates tended to be associated with initial lower elevations.

Large-scale (kilometers) longshore variations in the dune crest elevation changes and volume change are apparent in Figure 6. Wherever the dune crest was more than about 0.5 m above the wrack line, little or no erosion occurred (for example, the beige area 1 in Figure 6). In contrast, where the initial elevations were lower or the primary dune line was absent (pink area 2, Figure 6), erosion rates were greater.

Table 2. Summary of volume measurements. Volumes for the island platform, beaches, and total (combined), as well as the fraction of the initial (pre-Dorian; 30 Sep) volume, are tabulated for three different methods for replacing missing data (see text). Mean elevation (volume / area) for the platforms and the beaches are tabulated for the empirical Bayesian kriging (EBK) method only. Values for the -1 surface fall between the values for the 0 and -2 surfaces, and the Gauss values are similar to the EBK values.

	Platform Volume (Mm^3)			**Beach Volume (Mm^3)**			**Total Volume (Mm^3)**			**Fraction of Initial Total Volume ( )**			**Plat. Elev. (m)**	**Beach Elev. (m)**
Method	0	-2	EBK	0	-2	EBK	0	-2	EBK	0	-2	EBK	EBK	EBK
30 Aug	12.52	12.50	12.52	4.07	4.07	4.07	16.59	16.57	16.59	1.00	1.00	1.00	1.92	1.78
12 Sep	10.92	10.78	11.09	2.51	2.50	2.56	13.43	13.33	13.65	0.81	0.80	0.82	1.70	1.81
11 Oct	10.78	10.30	10.61	2.72	2.65	2.70	13.50	12.95	13.31	0.81	0.82	0.80	1.63	1.65
26 Nov	11.22	11.07	11.18	2.73	2.72	2.71	13.95	13.78	13.89	0.84	0.84	0.84	1.72	1.47

During the initial post-storm interval (September to October), the subaerial volume of North Core Banks continued to decrease slightly to 13.3 ± 0.9 Mm^3 on October 10-11, which is a 2% reduction. This was not significant considering the uncertainty in the DSMs (Figure 12) and is likely an artifact of the higher water levels during the October survey. Table 2 shows that these small losses were related to a decrease in platform volume; beach volumes actually increased slightly, and this gain was related to an increase in beach area (Figure 12b; Table 2) despite the shoreline retreat evident in Figure 7b and discussed below. This suggests that while the beaches in October were generally narrower, they were more continuous across the eroded channels and slightly higher than in September.

The small losses during the first month post-storm were recovered during the second month, as a subaerial volume of 13.9 ± 0.9 Mm^3 was measured in November 2019, which was a 4% increase from the previous survey (Figure 12a), associated with increases in both island platform and beach volumes. Difference maps show washover wedges that had prograded into the washout channels, raising elevations from subtidal to 1.5 – 2.5 m (Figure 11). These deposits had berm crests as high as 2.7 m, usually located where the channel incised the dune, and tapered landward, often with an abrupt termination at the leading edge (Figure 10). Little evidence of net longshore transport, such as spits or offset channels, was visible and we hypothesize that most of the sediment that contributed to the subaerial volume increase was sourced from the adjacent nearshore.

3.4 Shoreline changes

The ocean-side shoreline, defined by the seaward-most location of the MHW (0.4-m) contour, exhibited less change than might be expected during Hurricane Dorian, given the large waves generated by this storm (Figure 2) and large loss of island volume documented in Section 3.3. Most change occurred near the re-entrants associated with washout channels. However, in area 1 – containing almost no washout channels (Figure 8) – the shoreline position was nearly unchanged by Hurricane Dorian (Figure 7). The entire shoreline change was landward, -4.57 m ± 6.66 m (alongshore mean ± std. dev.; negative values indicate landward or erosional change) between August 30 to September 12-13. Within area 1, the shoreline change was only -0.88 m ± 3.75 m, compared to an average of -5.07 m ± 6.81 m elsewhere. In the weeks after Hurricane Dorian, a greater range of shoreline retreat and progradation occurred, focused again near the washout channels, for an average shoreline change of -5.07 m ± 15.08 m between the post-Dorian and October surveys. The final survey interval between October and November 26 included a powerful nor'easter with 8-m waves recorded at 0340 UTC on 17 November at the Diamond Shoals buoy. Shoreline change in this time period varied along the island with a small net seaward shift of 1.02 m ± 18.77 m, focused mainly on area 1 (Figure 7). A slight increase in beach volume in this interval was associated with a substantial increase in beach area (Figure 12). Examination of the orthomosaics shows the berms were more alongshore uniform, closing most of the eroded channels to form ponds. The island-averaged shoreline location was at

its most eroded state one month following the passage of Hurricane Dorian, although the spatial variability of the shoreline change was high (Figure 7).

3.5 Areal analyses of washout and washover features

Areal analysis indicated that incised outwash drainages occupied ~1.11 Mm^2 in the post-Dorian imagery. This is about 16% of the 8.79 Mm^2 island platform + beach area defined in Section 2.2. We identified 86 distinct features (Figure 8; Table 3) ranging

Table 3. Distribution of morphometry metrics for outwash (Hurricane Dorian) and overwash (Hurricane Florence) features.

	Outwash n = 86				**Overwash n=111**			
	Mean	*Median*	*Min.*	*Max.*	*Mean*	*Median*	*Min.*	*Max.*
Area (m^2)	12,857 ± 16,234	7,390	46	89,088	12,673 ± 26,028	4,651	146	220,349
Length (m)	169 ± 107	148	11	474	242 ± 476	140	33	4,267
Width (m)	115 ± 83	106	7	366	97 ± 61	83	14	344
Throat (m)	62 ± 57	52	5	360	99 ± 157	42	4	1,000
Perimeter (m)	1,739 ± 1,561	1,340	36	5,991	1,566 ± 3,000	872	158	30,259
Distortion Index*	3.84	3.78	1.31	6.74	0.09	0.07	0.00	0.32
Area outside of co-located overwash (%)	36	34	0	81				

broadly in area from 4 m^2 to 89,000 m^2 (mean ± std. dev. was 12,857 ± 16,234 m^2). Only four drainage features connected across the island to the sound, and these occupied pre-existing marsh channels. Lengths ranged from 11 to 474 m and the mean (median) length was 169 m (148 m) and widths ranged from 7 to 366 m and the mean (median) width was 115 m (83 m). The mean (± std. dev.) width/length ratio was 0.6 (±0.26). The width of the throats, defined here as the width of the outwash channel throats through the gaps in the primary dune line, ranged from 5 to 360 m, with mean (median) widths of 62 m (52 m). The

distribution of most of these statistics was approximately log-normal, so the statistics are skewed by a few very large features.

The apparent co-location of the washout drainages and the antecedent washover fans motivated us to compile analogous metrics for the post-Florence washover fans, mapped as described in Section 2.7. The 111 fans we identified occupied 1.19 Mm^2, 7% more area than the drainage features. Fan areas ranged from 146 to 220,349 m^2 (area mean: 12,673 m^2, median: 4,651 m^2). Lengths ranged from 33 m to 4,267 m (length mean: 242 m, median: 140 m. Widths ranged from 14 m to 344 m (width mean: 97 m, median 83 m). Comparison of the distribution of areas for drainages and fans (not shown) indicates that, while the washover fans had an approximately log-normal distribution, the washout drainage area was bimodal, with peaks at ~5,000 m^2 and ~10,000 m^2. However, a Mann-Whitney U test indicates we cannot reject the null hypothesis that the two distributions are equal (p=0.64).

All washout drainages were associated with washover fans. But not all the washover fans contained washout features. Almost all (95%) washout drainages extended beyond the antecedent washover fans. On average, only 64% of each drainage area occupied an overwash fan; the remaining 36% of the drainage area eroded beyond the limits of the associated fan. In these cases, knickpoints had eroded beyond the sparsely vegetated fans into regions with denser and taller vegetation. This tendency for erosion to transgress the boundaries of washover fans indicates that the better-established vegetation does not entirely prevent incision by outwash, but it is unknown whether vegetation acts to slow that process.

The relationship between A and L was well described by linear fits in log-log space for both post-Dorian washout drainages (r^2=0.939) and washover fans (r^2=0.797) from several studies (Hudock, 2014; Lazarus et al., 2016; 2020) with similar slopes ± std. error of 0.582 ± 0.012 and 0.576 ± 0.014, respectively (Figure 8c). This relationship was also similar to that found by Lazarus (2016) for laboratory washover lobes and associated drainage features (which he called “throats”, differing from our use of the term). These data are also plotted on Figure 8c. Thus, our data contribute additional support for the results of Lazarus (2016) and Lazarus et al. (2020): there is an allometric symmetry found among the

washover and drainage features over scales ranging from cm to km. Taken together, these results suggest that the general shape and scaling laws apply for both source (washout drainages) and sink (washover deposits) features, and these features mirror each other.

Lazarus et al. (2020) also found consistency in the relationship between the area and volume (i.e., the average thickness) of washover fans. We find the same linear relationship in log-log space between the area and eroded volume (i.e., average depth) of the washout drainages (Figure 8d). The excellent fit (r^2 = 0.990), with a slope of 1.003 ± 0.013 indicates the average depth of the drainage features is about 1 m, with a slight tendency for larger features to be shallower.

The distributions of outwash and overwash distortion index DI (Figure 8e) show that the three main outwash shapes (tapering, lobate and apron) have distinctly different complexities that increase in that order. When all the outwash shapes are taken together, the mean (median) 3.84 (3.78) DI values were higher than those of washover fans, which had a mean (median) value of 3.60 (3.17), and a Mann-Whitney U test indicates the distributions were significantly different (p=0.011). Therefore, we can conclude that the washout drainages were generally more dendritic while washover fans were more lobate.

4 Discussion

4.1 Magnitude of erosion

The erosion of North Core Banks by sound-side flooding is remarkable for its magnitude. The outwash removed an average of 117 m^3/m from the 36-km barrier, with much higher losses on some transects. Except for erosion during Hurricane Sandy, this is a factor of five to ten time larger than most reported volume losses from beaches and dunes during ocean-side storms (Table 4). The island-wide average is smaller than the maximum erosion rates for 10-m stretches, with loss rates of >200 m^3/m, observed during Hurricane Sandy in 2012 (Sopkin et al., 2014). Hurricane Dorian losses, which occurred over a few hours, are comparable to cumulative erosion measured over longer stormy periods, like the losses from Southern California beaches during the 2015–2016 El Niño (Young et al., 2018). Furthermore, the erosion was not mitigated by washover deposits, as often happens during ocean-side erosion events. For example, Hapke et al. (2013) estimated that deposition in

washover deposits represented 14% of the sand lost from the beach and dunes during Hurricane Sandy.

4.2 Colocation and symmetry of washout drainages and antecedent washover fans

Much of the area occupied by washout drainages formed during Hurricane Dorian coincided with washover fans formed during Hurricane Florence. Specifically, all washout features overlapped to some extent with earlier washover features. A small portion of

Table 4. Reported erosion rates from various storms.

Location	Storm(s)	Volume loss (m^3/m)	Reference
Latvia (Gulf of Riga)	Unnamed hurricane (2005)	5 – 15	Eberhards et al., 2006
Topsail Beach, NC	Hurricane Hugo (1989)	18	Wells and McNinch, 1991
U.S. East Coast	Hurricane Sandy (2012)	>200	Sopkin et al., 2014
Central Florida Atlantic Coast	Hurricane Floyd (1999)	18	Zhang et al., 2005
Florida Panhandle	Hurricane Dennis (2005)	18 – 25	Priestas and Fagherazzi, 2010
Florida Panhandle, SE Florida	Four hurricanes in 2004	11 – 66	Sallenger et al., 2006
Northern France	Storms in 2012 and 2014	14 – 24	Héquette et al., 2019
Narrabeen-Collaroy beaches, NSW	East Coast Low (2011)	24	Splinter et al., 2018
West-central Florida	Tropical Storm Eta (2020)	10 -13	Cheng et al., 2021
Fire Island, NY	Hurricane Sandy (2012)	35 – 59	Hapke et al., 2013
North Core Banks, NC	Hurricane Dorian (2019)	117 (mean) 0 – 440	This study

washover features showed no evidence of subsequent incision by outwash. The washout drainages covered approximately the same area and had similar, but slightly more convoluted shapes. Most extended landward slightly beyond the borders of washover

929 deposits. There are several possible explanations for the colocation and symmetry. One is
930 that fresh washover fans were more easily eroded, but this explanation is weakened by the
931 observation that the fan characteristics had changed in the 11 months since Hurricane
932 Florence. Pre-Dorian orthomosaics and DSMs show that Hurricane Florence fans became
933 moderately vegetated, and that incipient dunes and blowouts had formed on their surfaces,
934 which were no longer topographically smooth. The fans no longer exhibited the fresh
935 appearance seen in the post-Florence images and were sometimes hard to distinguish from
936 the broader washover platform. Furthermore, many of the erosional channels cut by
937 outwash during Hurricane Dorian extended into denser back-barrier vegetation, beyond the
938 bounds of the recent washover fans, suggesting that vegetation did not substantially hinder
939 outwash erosion during Hurricane Dorian. Another explanation for feature colocation is
940 control by gaps in the primary dune line. A unifying characteristic of both the depositional
941 washover fans and the erosional washout channels was connection to the beach via dune
942 breaches with elevations lower than ~2.5 m. We suggest that the colocation of the
943 depositional and erosional features was controlled by the gaps in the foredunes that
944 conveyed overwash onto the barrier platform during Hurricane Florence and acted as initial
945 conduits for floodwaters from the inundated barrier platform to the sea during Hurricane
946 Dorian.

947 Although gaps in the dune line can explain the colocation of washover and washout
948 features, they do not explain the similarity in metrics for shapes and allometry. Although
949 Lazarus (2016) notes that the symmetrical, scale-invariant empirical relationships do not
950 demonstrate mechanisms, they might suggest that the mechanisms are similar. The
951 hydrodynamics of overwash through gaps in the dune line with elevation d_c varies with
952 relative total water levels determined by the surge height S and the runup height R
953 (Donnelly et al. 2006). During the runup overwash regimes, when $S < d_c$ but combined $R+S$
954 $\geq d_c$, incident waves and infragravity motions deliver individual pulses of water over the
955 beach crest or gap in the dunes. In the inundation regime, where $S > d_c$, a relatively constant
956 flow of water is supplied over the dune crests. In both cases, however, flow down the fans
957 that form on the landward side tends to resemble open-channel flow pulsating at
958 infragravity-wave frequencies modulated by very low-frequency fluctuations (Anarde et al.,

2020) and can be represented by the Chezy formula (Sánchez-Arcilla and Jimenez, 1994). Outwash is also characterized by open-channel flow dynamics. Thus, we propose that the similarity in shapes of washout drainages and washover deposits arises because both processes are governed by gradients in the free water surfaces that connect the dune gaps with a region of drainage influence.

4.3 Discharge and sediment flux

We made approximate quantitative estimates of outwash flow velocity and sand transport using the measured channel geometries and estimated water-surface slope. We reasoned that the water-surface slope η was approximately $1/300$, based on the elevation at the head of the drainages and the distance to the ocean. We used the open-channel flow equation (e.g., Dyer, 1986) with a Manning's n of 0.025 s m$^{-1/3}$ (Chow, 1959; Soulsby, 1997) to estimate instantaneous depth-averaged flow velocity $U = \frac{1}{n} R_h^{2/3} \eta^{1/2}$ m s^{-1} where R_h = $A_c/(2h_c+b)$ (m) is the hydraulic radius for a rectangular channel, A_c (m^2) is the cross-sectional channel area, h_c (m) is the average channel depth, and b (m) is the channel width. Channel geometry parameters A_c, h_c, and b were calculated for all gaps in the primary dune line with elevations less than 2.5 m, deeper than 0.5 m, and with A_c > 5 m^2. There were 86 of these channels with h_c ranging from 0.5 m to 3 m with mean (median) of 1.6 (1.6) (Figure 13) and A_c ranging from 5.6 to 572 m^2, with a mean (median) cross-sectional area of 112 (85) m^2. Estimated instantaneous flow velocities for individual channels ranged from 1.3 to 4.6 m s^{-1}, with a mean (median) of 2.9 (3.0) m s^{-1} (Figure 13). These flows were close to supercritical (i.e., approaching the speed of shallow-water waves), with Froude numbers $F_r = U/\sqrt{gh_c}$ (dimensionless) ranging from 0.6 to 0.9. Water discharge rates (UA_c) through the individual channels ranged from 8 to 1,790 m^3 s^{-1} and the total instantaneous discharge rate summed over all channels was 32,160 m^3 s^{-1}, or about twice the average discharge rate of the Mississippi River.

Bed stress τ_b (Pa) was estimated as $\tau_b = C_d \rho_w U^2$ where $C_d = gn^2/h_c^{\frac{1}{3}}$ (Soulsby, 1997, eqn 31) and ρ_w = 1,027 kg m^{-3} is water density. C_d ranged from 0.004 to 0.008, with a median value of 0.005. Bed stresses ranged from 14 to 94 Pa, with a median of 49 Pa. Bedload and suspended-load volumetric transport rates q_b and q_s (m^3 m^{-1} s^{-1}) were

988 calculated using the van Rijn (1984) formulae described in Soulsby (1997; his equation
989 133) using a median grain size D_{50}= 0.43 mm and D_{90} = 1 mm, corresponding to a sample
990 from South Core Banks (Hovenga et al., 2019). Spatially smoothed instantaneous bedload
991 transport rates ranged from 0 to 0.023 $m^3\ m^{-1}\ s^{-1}$ with median of 0.006 $m^3\ m^{-1}\ s^{-1}$, and
992

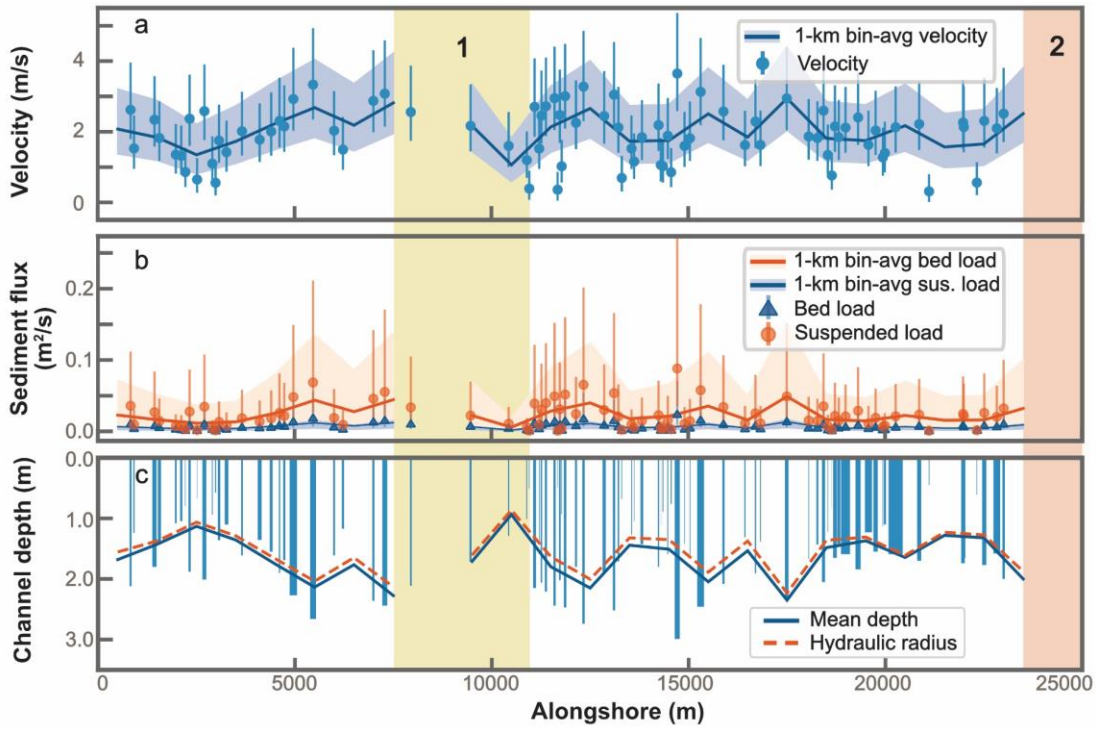

993

994 **Figure 13. Estimates of outwash flow velocities and sediment-transport rates in**
995 **channels cut through the primary dune line at the peak of the flood event during**
996 **Hurricane Dorian. a) estimated depth-mean current speeds *U*. b) estimated bedload**
997 **(Q_b) and suspended (Q_s) volumetric sediment fluxes. In both panels, dots indicate**
998 **values for individual channels and vertical bars indicate uncertainties based on a**
999 **range of assumed water-surface slope and bed roughness. Lines and shaded regions**
1000 **indicate mean and standard deviation of values bin-averaged over 1,000 m. c) Mean**
1001 **depths h_c and hydraulic radii R_h of channels incised across the primary dune line**
1002 **during Hurricane Dorian. Bars are scaled by channel widths; h_c and R_h are bin-**
1003 **averaged over 1000-m intervals. Areas 1 and 2 as in previous figures**.

1004 suspended transport rates ranged from 0.001 to 0.088 $m^3\ m^{-1}\ s^{-1}$ with a median of 0.019 m^3
1005 $m^{-1}\ s^{-1}$. (Figure 13). We multiplied transport rates for each channel by the channel widths
1006 and summed over all channels to estimate a total, island-wide instantaneous transport rate
1007 of 0.69 million $m^3\ h^{-1}$. At that rate, assuming in situ porosity of 0.35, it would take about 2.7

h to remove the ~2.9 Mm^3 of sand lost during Dorian. These numbers are sensitive to our many assumptions, but they illustrate the magnitude of this event.

4.4 Prospects for geomorphic recovery

From a morphological perspective that accounts only for sand volume, full recovery of North Core Banks will occur when the ponds and depressions have been filled, the washover platform is restored to pre-hurricane elevations, and the subaerial island volume approximates the pre-Hurricane Dorian volume. The initial recovery processes included bar migration and spit growth (Figures 4, 5, 10, and 11) but, once a continuous berm has been established, sediment can only be delivered to the ponds in a few ways: overwash, aeolian transport, transport by sound-side flooding, transport during pluvial runoff events, and in situ generation of biogenic material. Significant (but still small) gains in island volume occurred between the October and November surveys. The November survey followed a strong nor'easter when significant wave heights of ~8 m with dominant periods of ~15 s were measured at the Diamond Shoals buoy. That survey revealed a nearly continuous berm that closed off the washout channels with berm elevations ranging from 1.2 to 2.4 m (Figures 10 and 11). Landward of the berm, the washout features were partially filled with washover sand. But to continue to fill these ponds with washover sand, additional overwash events must overtop the berm, which will require either a) total water levels (tide + surge + setup + swash) to reach or exceed those elevations or b) lowering of the berm, followed by more moderate overwash events.

Conditions that could generate runup sufficient to overtop the higher berms are relatively infrequent. Assuming all runup events occur at high tide (mean higher high water = ~0.5 m) and are accompanied by a 0.5-m storm surge (which, combined, account for 1 m of the total water level), the probability of the run-up reaching the crest can be computed using the Stockdon et al. (2006) formula and hourly wave data from Diamond Shoals. Based on the November DSM, the likelihood of runup reaching the berm crest is higher for the wider channels, which have lower berm crests. For the lowest berms, conditions conducive to overwash occur in 47% of the hourly wave records. By contrast, conditions that will overtop the highest berms occur in less than 6% of the records. The actual occurrence is

likely to be much lower because these calculations assume high tide and constant surge of 0.5 m and ignore wave direction. The conclusion is that the recovery is likely to continue more frequently in the wider and more voluminous drainage features and less frequently in the smaller features with generally higher berms. The more complicated process of berm lowering and subsequent overwash, and the other mechanisms for filling the ponds, can be evaluated with continued monitoring using aerial photogrammetry and satellite imagery.

4.5 Sediment budget and island migration

Barrier islands survive in times of rising sea level by migrating landward and upward over centuries and millennia through processes of overwash, inlet migration, and aeolian transport (e.g., Leatherman, 1979; McBride et al., 2013). If a barrier island maintains a constant volume as it transgresses, its volume centroid must move up at the rate of relative sea-level rise v_z = SLR. If the island is migrating across a sloped surface, such as a linear shelf/back-barrier surface with slope α (e.g., Lorenzo-Trueba & Ashton, 2014), the rate v_x of landward translation required to achieve the required elevation gain is given by $v_x = -v_z / \tan\alpha$ in a coordinate system where seaward migration is positive.

We used elevation profiles extending across from Pamlico Sound, North Core Banks, and the inner continental shelf to estimate tan α, and found that it ranges from approximately $\alpha_1 = 8{\cdot}10^{-4}$ m/m on the shelf to $\alpha_2 = 2{\cdot}10^{-4}$ m/m across Pamlico Sound. Assuming SLR $\sim 2{\cdot}10^{-3}$ my^{-1}, the island must migrate landward at a rate v_x ranging from -2 to -10 my^{-1}. Actual rates of North Core Banks migration can be estimated from spatially averaged shoreline change rates on the ocean side, which have been determined from repeat transect measurements between 1961 and 2001 and varied from -20 to +6 my^{-1}, depending on the period of observation (Riggs and Ames, 2007). For the longest observation period (1946-1998), the overall average rate of North Core Banks was -1.3 my^{-1} (Riggs and Ames, 2007). Much higher rates (as much as -69 my^{-1}) were observed on individual transects, notably those near ephemeral inlets. The shoreline movements are accompanied by elevation increases with average rates of about 0.04 my^{-1} that are generally highest near the shore (0.03 – 0.06 my^{-1}) and decrease to 0.02 – 0.05 my^{-1} at a distance approximately 60 m inland from the shoreline (Riggs and Ames, 2007). These

numbers suggest that North Core Banks has been accreting vertically at rates that exceed sea-level rise but, during their short observation interval, was on the slow end of the necessary landward migration rate.

The sand washed out of the island and deposited on the shoreface during Hurricane Dorian would have caused a seaward and downward shift in the volume of the island, exactly the opposite of the movement needed to maintain subaerial integrity. We cannot estimate the magnitude of this shift precisely because we do not know exactly where the sand was deposited, but we can argue that the seaward shift is likely to be more than would occur during a typical ocean-side erosion event, for three reasons. First, the sand was sourced from farther inland, largely landward of the primary dune line. In contrast, typical ocean-side erosion events will remove sand primarily from the beach and dune toe (e.g., Brenner et al., 2018). Second, ocean water levels during Hurricane Dorian were set down by offshore winds. During most ocean-side erosion events, water levels are elevated by storm surge. Thus, if the locus of deposition of sand is primarily governed by water depth, the deposits during Hurricane Dorian would have occurred farther offshore. Third, the offshore transport of sand was driven by concentrated hydraulic jets that appear to be near supercritical (see Section 4.3), which would result in the building of sand lobes far offshore (Fagherazzi et al., 2015), rather than the more uniform offshore bar formation from ocean-side erosion. While there are considerable unknowns in these hypotheses, especially with respect to the location and depth of offshore sand transport and the rates of subsequent onshore movement of sand during recovery, outwash events introduce a unique offshore shift in the island volume centroid that represents a setback to long-term landward migration.

4.6 Synthesis model of the morphodynamics of outwash events

The measurements shown here provide a clear example of how outwash events can reshape a barrier island by distributing sand offshore during the rapid and energetic flooding across these islands. Washout channels carved into the islands soon become topographic depressions in the island landscape as coastal sediment transport closes the

channel mouths, which at North Core Banks resulted in numerous new ponds behind the island dunes.

However, outwash events are only one of the diverse types of sediment transport events that act to shape barrier island morphology. Many outwash events have been recognized (e.g., Hayes, 1967; Morton and Paine, 1985; Lennon, 1991; Bush and Pilkey, 1994; Goff et al., 2010; Sherwood et al., 2014; Passeri et al., 2018; Goff et al., 2019; van der Lugt et al., 2019) and recent rapid-response imagery (Over et al., 2021a) shows at least some evidence of outwash in most (23 of 32) storms. However, it is still not clear how often outwash events occur, how much landscape they affect, and what long-term role they play in barrier morphodynamics, compared with ocean-side and aeolian transport events that move sand much more regularly throughout time (e.g., Hosier and Cleary, 1977). Thus, the occurrence of outwash events needs to be placed in context with these more frequent – and perhaps more important – transport phenomena.

We have developed a simple conceptual model to relate these different types of morphologic events and how they may act on different island morphologies. Specifically, we compare a barrier island setting with limited backwater lagoon with one more similar to North Core Banks, which has a broad backwater sound (Figure 14). Initially, both settings have continuous but uneven primary dune lines that are susceptible to overwash at their low points when ocean conditions generate total water levels (tides + storm surge + wave setup + wave runup) that exceed the dune crests (Figure 14a). Overwash transports sand onto the barrier platform, depositing it as washover fans and coalescing washover platforms (Figure 14b). After the storm, initial recovery can occur through onshore bar migration and berm building, and longer-term recovery can occur through aeolian transport and accretion aided by vegetation growth (Figure 14c). To this point, processes are similar in both settings and dominated by oceanic conditions, but when strong offshore winds occur, the barrier with a broad lagoon can be flooded from the back side by wind-driven storm surge. If water levels are high enough, they will inundate the low-lying back of the island and seek outlets to the ocean through the gaps in the dunes created earlier by overwash (Figure 14d). With offshore winds, ocean water levels may be set down, creating steep water-level gradients from the flooded back side to the ocean, producing powerful

1124 flows that rapidly carve drainage networks out of the island platform. The sand is
1125 transported through the gaps, possibly by supercritical flows, and deposited in the
1126 nearshore, possibly as small wave-dominated deltas. Meanwhile, only minor morphological
1127 changes, maybe some aeolian transport and dune building, occur on the barrier with no
1128 lagoon. After the storm, the washout channels created on the barrier with the lagoon are
1129 closed by alongshore transport (spit building) and/or onshore transport (berm building),
1130 and the erosional scars become ponds (Figure 14e). However, the initial gaps in the
1131 primary dune line still exist, and the relatively low-lying berms that fill these gaps remain

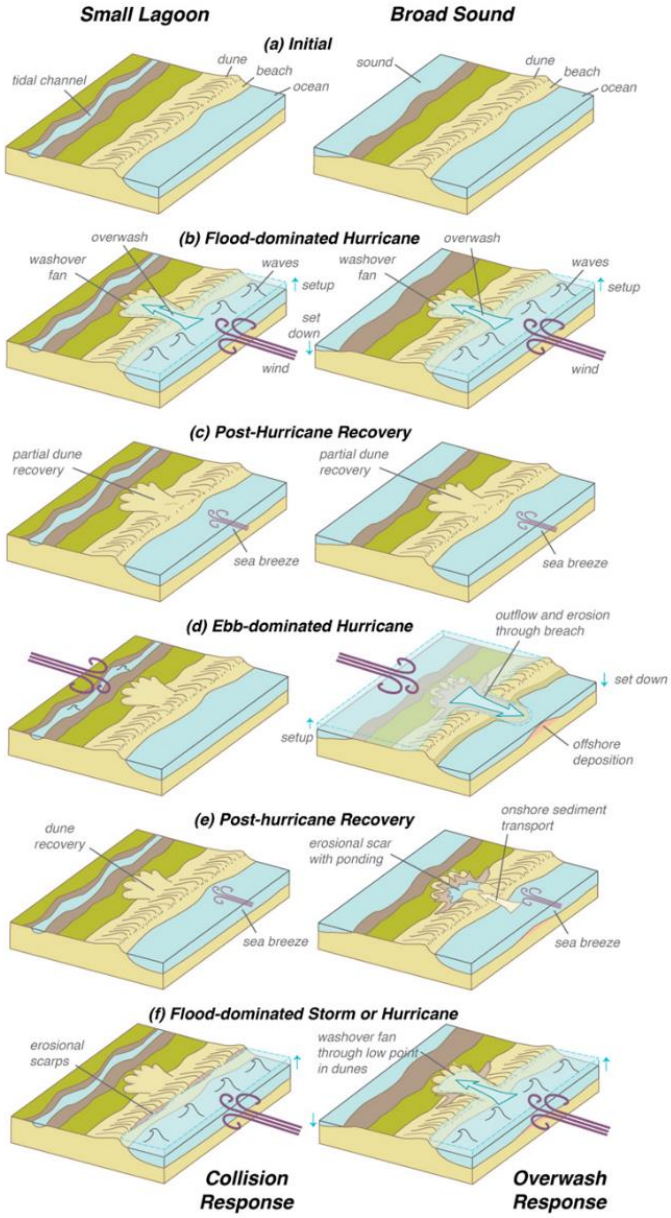

Figure 14. Conceptual model comparing evolution of barrier island settings without (left column) and with (right column) broad back-barrier water bodies (bays, lagoons, sounds, marsh estuaries).

susceptible to overwash. The barrier with no lagoon, on the other hand, may have built enough dune elevation so that most morphologic change is caused by dune erosion during collision (Figure 14f).

The fate of the sand eroded from the outwash channels is unknown, and so the conceptual model is incomplete. The sand may be deposited in relatively shallow water and thus remained available for transport back to shore (e.g., Morton and Paine, 1985) or to be swept away by alongshore transport. Or, it may be sequestered in deep water, beyond the zone of normal transport, like the sands eroded by hurricanes in Texas (Hayes, 1967; Gayes, 1991; Goff et al., 2010). The ultimate fate of the eroded sand has implications for the morphological evolution of the entire barrier chain. Future modeling or investigations of nearshore stratigraphy (e.g., Wei & Miselis, 2022) could yield more insight into the fate of these sands.

How frequent are outwash events? Over et al. (2021a) demonstrate that they occur somewhere in the U.S. almost yearly. At least one similar event has occurred in the historical record on North Core Banks: an unnamed storm in 1933 overwashed Core Banks from the sound side and opened the original Drum Inlet that demarcated North Core Banks (Barnes, 2013). Regionally, two of the three main inlets through the Outer Banks (Hatteras and Oregon Inlets) were formed during sound-side flooding in 1846 (Clinch et al., 2012; Barnes, 2013). The original New Inlet on Pea Island, NC, was opened during a nor'easter in 1932 that generated 12 ft (3.7 m) of surge in the sound (Markham, 1935, cited in Clinch et al., 2021; Safak et al., 2016). In 2010, the nearby New New Inlet formed through an existing washover gap in the dune formed during hybrid storm Nor'Ida (2009), driven by 2.6 m of sound-side surge generated by Hurricane Irene. Notably, no breaching or significant erosion occurred when Hurricane Emily (1993) generated ~2.6 m of sound-side surge near Buxton (Bush et al., 1996) because of the tall and continuous dunes there, highlighting the role of antecedent low spots along the dune line. However, the number of these events in the historical record suggests they are frequent enough to affect transgression rates over geologic time.

4.7 Habitat creation

Many coastal species have evolved to survive in early successional habitats largely created and maintained by storms. For example, throughout their Atlantic Coast breeding range, piping plovers preferentially select minimally vegetated areas with substrates that

are a mix of sand and shell (Zeigler et al., 2021) – conditions created through storm overwash (Zeigler et al., 2019). Nesting pairs in the southern portion of their Atlantic Coast breeding range were five times more likely to establish nests on washover deposits than on other coastal features (e.g., backshore areas and dunes; Zeigler et al., 2021). Piping plovers quickly colonized newly created overwash features on Fire Island, New York, USA after Hurricane Sandy (Zeigler et al., 2019), ultimately resulting in increased population productivity and size in the years following the storm (Robinson et al., 2019). Similarly, seabeach amaranth – an annual plant – prefers topographically homogenous, minimally vegetated overwash flats and beaches. Storms create these preferred conditions while also eliminating competition (i.e., with plants less disturbance-adapted), dispersing seeds, creating seed banks, and exposing seeds for germination (Sellars & Jolls, 2007).

Although erosion at North Core Banks resulted in an initial loss of the subaerial island footprint, the creation of new washover features and maintenance of existing features created during Hurricane Florence likely preserved high-quality habitat for a variety of species that utilize early successional habitats, including piping plovers, other shorebirds, and seabeach amaranth. The number of piping plover nesting pairs increased by 45% between 2020 and 2021, and managers hypothesize that a time lag occurred as piping plovers recolonized new habitats that were restructured by Hurricane Dorian (Altman & Stephenson, 2021). Likewise, the 2021 breeding season produced record high productivity and nest success for American oystercatchers *(Haematopus palliates)* and a record number of least tern (*Sternula antillarum*) and Wilson's plover (*C. wilsonia*) breeding pairs—trends that have been attributed to habitats created during Hurricanes Florence and Dorian (Altman & Stephenson, 2021)

Perhaps more importantly, flooding from the sound side by Hurricane Dorian increased foraging habitat for piping plovers and other shorebirds. Prior to fledging, many shorebird chicks are precocial, meaning they find food for themselves but must do so on foot without the ability to fly yet. Easy access over short distances between ocean-front nest sites and foraging areas with moist substrates along low-energy shorelines (e.g., shorelines along the back-barrier, inlets, and interior ponds) is critical for chick survival, and nests are more likely to be found near these foraging areas (Zeigler et al., 2021). The

newly created ponds and wet depressions situated behind the dunes, and adjacent to both washover deposits and back-barrier marsh, provide an ideal combination of foraging territory near potential nesting sites for shorebirds and colonial waterbirds. Furthermore, the first examination of these ponds (Cadell et al., 2021) shows they are different than the pre-existing marsh ponds. They are more saline, have higher pH and dissolved oxygen, and host different species of fish. This newly expanded habitat will evolve as the ponds eutrophy and sediment from overwash, pluvial runoff (Cadell et al. 2021), and possibly more back-barrier flooding continues to fill them. The character of this habitat will change, and the areal extent will slowly decrease as the island recovers but, as discussed above, that process is likely to take many years.

In addition to the beneficial impact of Hurricane Dorian on individual species, the storm-driven landform changes and processes documented in this study have broader implications for coastal ecosystem characteristics and resilience on North Core Banks. Connectivity and long-distance interactions among coastal ecosystems play important roles in maintaining ecosystem form and function (van de Koppel et al., 2015; Liebowitz et al., 2016). Some have argued that these individual ecosystems may be better described as a single “meta-ecosystem” or “coastal ecosystem mosaic,” connected by the flow of energy, materials, and organisms across ecosystem boundaries (Loreau et al., 2003; Sheaves, 2009). Connectivity also allows coastal landforms to respond dynamically to SLR and storms as opposed to being permanently inundated (Lentz et al., 2016). The combined reshaping of the island along with the creation of new salt ponds by overwash and outwash events generate habitat diversity that may translate to greater biodiversity and ecosystem resiliency that can be maintained while islands like North Core Banks migrate and gain elevation with SLR (e.g., Walters & Kirwan, 2016; Lorenzo-Trueba & Mariotti, 2017). In addition, sandy beaches typically lack organisms responsible for primary production and instead rely on nutrient subsidies from the ocean or bay/sound, such as phytoplankton and macrophytes. These organisms, which have appeared in the new ponds (Cadell et al., 2021) provide nutrition for secondary producers (e.g., amphipods and other invertebrates; Michaud et al., 2019), ultimately supporting a food web that propagates up to shorebirds and other large vertebrates (reviewed in Liebowitz et al., 2016;). Few studies have

examined the combined influence of overwash and outwash events on ecosystem form, function, or resiliency. Combined overwash and washout events may lead to greater biodiversity associated with ecosystem connectivity, which could promote more resilient barrier island ecosystems.

5 Conclusions

We used aerial imagery, photogrammetry products, model simulations, and field observations to study the mechanisms by which a hurricane reshaped a barrier island on the Outer Banks of North Carolina. The exceptional erosion that occurred on North Core Banks was the result of a sound-side flood event driven primarily by winds during Hurricane Dorian. Erosion rates were nearly an order of magnitude higher than rates observed during severe ocean-side storms, and most of the sand was removed from the core of the island platform, rather than from beaches and dunes. As a result, shoreline erosion during the event was minimal. Gaps in the dunes facilitated the formation of washout drainages that mostly occupied former washover fans. Without gaps in the primary dune line, erosion from sound-side flooding would have been negligible. The ratio of volume/area of the washout features indicated a nearly uniform average depth of 1 m, mirroring a similar relationship for the thickness of washover deposits from a previous study. Initial recovery from this event included rebuilding of the beach through bar migration and bar and spit formation that partially closed the washout channels. Further recovery included berm building and overwash, sealing most of the washout channels to form ponds and partially filling them with washover deposits. The newly formed ponds, adjacent to both bare sands and vegetated areas increased the diversity and connectivity of habitats. The path to geomorphic recovery (i.e., restoration of the pre-Dorian island volume) is unclear and may be slow, possibly lasting a decade or more. We presented a conceptual model comparing barrier islands subject to sound-side inundation to more typical settings. No individual aspect of this model is novel, but it is a unique description of an unusual, but possibly important, sequence of processes in a barrier-island setting that has not been previously described. The event we describe here created beneficial habitat for rare and endangered species and may enhance biodiversity but represents a setback in

the sequence of overwash and aeolian transport required to build island elevation and drive the transgression required for a barrier island to maintain pace with rising sea level.

Acknowledgments

The authors have no conflicts of interest. This research was supported by U.S. Geological Survey (USGS) Coastal and Marine Hazards and Resources Program as part of the Remote Sensing Coastal Change project and by the Congressional Additional Supplemental Appropriations for Disaster Relief Act of 2019. We thank our partners at the National Park Service for field observations and valuable discussions. ADvanced CIRCulation (ADCIRC) ocean model results were provided by the Department of Homeland Security (DHS) Coastal Resilience Center at the University of North Carolina, Chapel Hill (adcircprediction.org). We thank Dan Ciarletta and a second USGS reviewer for valuable suggestions that improved an earlier draft, and we thank Drs. John Goff, Eli Lazarus, and Kristen Splinter for constructive review comments that have been incorporated in this version. Any use of trade, firm, or product names is for descriptive purposes only and does not imply endorsement by the U.S. Government.

Data Availability

NOAA NGS Emergency Response Imagery is available at https://storms.ngs.noaa.gov/storms/dorian/index.html.

Operational ADCIRC forecasts for Hurricane Dorian are available at http://tds.renci.org/thredds/catalog/2019/dorian/catalog.html

Topo/bathy lidar data are available on NOAA Digital Dataviewer: https://coast.noaa.gov/dataviewer/#/lidar/search/.

USGS imagery of North Core Banks has been published in the following data releases: Kranenburg et al., 2020, 2021a,b, 2022a,b.

Photogrammetric products (DSMs and orthomosaics) have been published in Ritchie et al., 2021, 2022.

Ground control points used in the SfM reconstructions have been published by Brown et al., 2021.

References

Altman, J., & Stephenson, C. (2021), *Shorebird monitoring and management at Cape Lookout National Seashores*. 2021 Annual Report. U.S. National Park Service. 43 pages. Available at: https://www.nps.gov/calo/learn/management/wildlife-management.htm

Anarde, K., Figlus, J., Sous, D., & Tissier, M. (2020), Transformation of Infragravity Waves during Hurricane Overwash. *Journal of Marine Science and Engineering*, *8*(8), 545. https://doi.org/10.3390/jmse8080545

Anderson, S., & Pitlick, J. (2014), Using repeat lidar to estimate sediment transport in a steep stream. *Journal of Geophysical Research: Earth Surface*, *119*(3), 621–643. https://doi.org/10.1002/2013JF002933

Anderson, S. W. (2019), Uncertainty in quantitative analyses of topographic change: error propagation and the role of thresholding. *Earth Surface Processes and Landforms*, *44*(5), 1015–1033. https://doi.org/10.1002/esp.4551

Avila, L. A., Stewart, S. R., Berg, R., & Hagen, A. B. (2020), *Hurricane Dorian (AL052019) 24 August – 7 September 2019*, Tropical Cyclone Report, 74 p. National Weather Service, National Hurricane Center.

Barnes, J. (2013). *North Carolina's Hurricane History* (Fourth Edition). Chapel Hill: University of North Carolina Press.

Breithaupt, B. H., Matthews, N. A., & Noble, T. A. (2004), An Integrated Approach to Three-Dimensional Data Collection at Dinosaur Tracksites in the Rocky Mountain West. *Ichnos*, *11*(1–2), 11–26. https://doi.org/10.1080/10420940490442296

Brenner, O. T., Lentz, E. E., Hapke, C. J., Henderson, R. E., Wilson, K. E., & Nelson, T. R. (2018), Characterizing storm response and recovery using the beach change envelope: Fire Island, New York. *Geomorphology*, 300, 189–202. https://doi.org/10.1016/j.geomorph.2017.08.004

1311 Brodie, K., Conery, I., Cohn, N., Spore, N., & Palmsten, M. (2019), Spatial Variability of
1312 Coastal Foredune Evolution, Part A: Timescales of Months to Years. *Journal of*
1313 *Marine Science and Engineering*, 7(5), 124. https://doi.org/10.3390/jmse7050124

1314 Brown, J.A., Sherwood, C.R., Martini, M., Kranenburg, C.J., and Over, J.R., 2021, *Ground*
1315 *control point data from the Outer Banks, North Carolina, post-Hurricane Dorian,*
1316 *September 2019*: U.S. Geological Survey data release,
1317 https://doi.org/10.5066/P9DVZC23

1318 Bull, W. B. (1975), Allometric change of landforms. *GSA Bulletin*, 86(11), 1489–1498.
1319 https://doi.org/10.1130/0016-7606(1975)86<1489:ACOL>2.0.CO;2

1320 Bush, D. M., & Pilkey, O. H. (1994), Mitigation of Hurricane Property Damage on Barrier
1321 Islands: A Geological View. *Journal of Coastal Research*, 311–326.

1322 Bush, D. M., Young, R. S., Webb, C. A., & Thieler, E. R. (1996), Soundside Impacts of a
1323 Northward Tracking Tropical Cyclone: Hurricane Emily (31AUG93), Cape Hatteras
1324 Area, North Carolina. *Journal of Coastal Research*, 12(1), 229–239.

1325 Cadell, S., Chen, Y., Daly, J., Evans, J., Herschfield, C., Hynes, J., et al. (2021), Ecological
1326 Functions and Ecosystem Services of Overwash Ponds on North Core Banks, NC (Fall
1327 2021 Capstone Report). UNC Institute of Marine Science Field Site, Morehead City,
1328 NC: University of North Carolina at Chapel Hill. 142 pp.

1329 Cairns, W. E. (1982), Biology and Behavior of Breeding Piping Plovers. *The Wilson Bulletin*,
1330 94(4), 531–545.

1331 Cassalho, F., Miesse, T. W., de Lima, A. de S., Khalid, A., Ferreira, C. M., & Sutton-Grier, A. E.
1332 (2021), Coastal Wetlands Exposure to Storm Surge and Waves in the Albemarle-
1333 Pamlico Estuarine System during Extreme Events. *Wetlands*, 41(4), 49.
1334 https://doi.org/10.1007/s13157-021-01443-4

1335 Cheng, J., Toledo Cossu, F., & Wang, P. (2021), Factors controlling longshore variations of
1336 beach changes induced by Tropical Storm Eta (2020) along Pinellas County beaches,
1337 west-central Florida. *Shore & Beach*, 75–85. https://doi.org/10.34237/1008929

1338 Chow, V. T. (1959), *Open-Channel Hydraulics*. New York, NY, USA: McGraw-Hill Book Co.

1339 Clinch, A. S., Russ, E. R., Oliver, R. C., Mitasova, H., & Overton, M. F. (2012). Hurricane Irene
1340 and the Pea Island Breach: Pre-storm site characterization and storm surge
1341 estimation using geospatial technologies. *Shore & Beach*, 80(2), 10.

1342 Clunies, G. J., Mulligan, R. P., Mallinson, D. J., & Walsh, J. P. (2017). Modeling hydrodynamics
1343 of large lagoons: Insights from the Albemarle-Pamlico Estuarine System. Estuarine,
1344 *Coastal and Shelf Science*, 189, 90–103. https://doi.org/10.1016/j.ecss.2017.03.012

1345 Cohen, J. B., Houghton, L. M., & Fraser, J. D. (2009), Nesting Density and Reproductive
1346 Success of Piping Plovers in Response to Storm- and Human-Created Habitat
1347 Changes. *Wildlife Monographs*, *173*(1), 1–24. https://doi.org/10.2193/2007-553

1348 Cohen, J., & Fraser, J. (2010), Piping plover foraging distribution and prey abundance in the
1349 pre-laying period. *The Wilson Journal of Ornithology, 122*, 578–582.
1350 https://doi.org/10.1676/09-145.1

1351 Conroy, S. J., & Milosch, J. L. (2011), An Estimation of the Coastal Premium for Residential
1352 Housing Prices in San Diego County. *The Journal of Real Estate Finance and*
1353 *Economics*, *42*(2), 211–228. https://doi.org/10.1007/s11146-009-9195-x

1354 Cowell, P. J., Stive, M. J. F., Niedoroda, A. W., Vriend, H. J. de, Swift, D. J. P., Kaminsky, G. M., &
1355 Capobianco, M. (2003), The Coastal-Tract (Part 1): A Conceptual Approach to
1356 Aggregated Modeling of Low-Order Coastal Change. *Journal of Coastal Research*,
1357 19(4), 812–827.

1358 Das, B. C., Islam, A., & Sarkar, B. (2022), Drainage Basin Shape Indices to Understanding
1359 Channel Hydraulics. *Water Resources Management*, 36(8), 2523–2547.
1360 https://doi.org/10.1007/s11269-022-03121-4

1361 Donnelly, C., Kraus, N., & Larson, M. (2006), State of Knowledge on Measurement and
1362 Modeling of Coastal Overwash. *Journal of Coastal Research*, *224*, 965–991.
1363 https://doi.org/10.2112/04-0431.1

1364 Durán Vinent, O., & Moore, L. J. (2015), Barrier island bistability induced by biophysical
1365 interactions. *Nature Climate Change*, 5(2), 158–162.
1366 https://doi.org/10.1038/nclimate2474

1367 Dyer, K. R. (1986), *Coastal and Estuarine Sediment Dynamics*. Chichester, West Sussex, UK:
1368 John Wiley & Sons.

1369 Eberhards, G., Lapinskis, J., & Saltupe, B. (2006), Hurricane Erwin 2005 coastal erosion in
1370 Latvia. *Baltica*, 19(1), 10–19.

1371 Esri Inc. (2021), *ArcGIS Pro* (Version 2.8.1). Software at https://www.esri.com/en-
1372 us/arcgis/products/arcgis-pro/overview. *Accessed and downloaded June 2021.*

1373 Fagherazzi, S., Edmonds, D. A., Nardin, W., Leonardi, N., Canestrelli, A., Falcini, F., et al.
1374 (2015), Dynamics of river mouth deposits. *Reviews of Geophysics*, 53(3), 642–672.
1375 https://doi.org/10.1002/2014RG000451

1376 Fisher, J. J. (1962) *Geomorphic expression of former inlets along the Outer Banks of North*
1377 *Carolina*. (PhD Thesis). University of North Carolina.

1378 FitzGerald, D. M., & Pendleton, E. (2002), Inlet Formation and Evolution of the Sediment
1379 Bypassing System: New Inlet, Cape Cod, Massachusetts. *Journal of Coastal Research*,
1380 (36 (10036)), 290–299. https://doi.org/10.2112/1551-5036-36.sp1.290

1381 Fraser, J. D., & Catlin, D. H. (2019), Habitat Ecology and Conservation of Charadrius Plovers.
1382 In *The Population Ecology and Conservation of Charadrius Plovers*. CRC Press.

1383 Garmestani, A. S., Percival, H. F., Portier, K. M., & Rice, K. G. (2000), Nest site selection by
1384 loggerhead sea turtle in Florida's Ten Thousand Islands. *Journal of Herpetology, 34*,
1385 504-510. https://doi.org/10.2307/1565263

1386 Godfrey, P. J., & Godfrey, M. M. (1976), *Barrier Island Ecology of Cape Lookout National*
1387 *Seashore and Vicinity, North Carolina.* National Park Service Monograph Series 9, U.S.
1388 Government Printing Office.Goff, J. A., Allison, M. A., & Gulick, S. P. S. (2010), Offshore
1389 transport of sediment during cyclonic storms: Hurricane Ike (2008), Texas Gulf
1390 Coast, USA. *Geology*, 38(4), 351–354. https://doi.org/10.1130/G30632.1

1391 Goff, J. A., Swartz, J. M., Gulick, S. P. S., Dawson, C. N., & de Alegria-Arzaburu, A. R. (2019), An
1392 outflow event on the left side of Hurricane Harvey: Erosion of barrier sand and
1393 seaward transport through Aransas Pass, Texas. *Geomorphology*, 334, 44–57.
1394 https://doi.org/10.1016/j.geomorph.2019.02.038Grzegorzewski, A. S., Cialone, M.

A., & Wamsley, T. V. (2011), Interaction of Barrier Islands and Storms: Implications for Flood Risk Reduction in Louisiana and Mississippi. *Journal of Coastal Research*, (59), 156–164. https://doi.org/10.2112/SI59-016.1

Hayes, M. O. (1967), *Hurricanes as Geological Agents: Case Studies of Hurricanes Carla, 1961, and Cindy, 1963* (Report of Investigations No. 61) (p. 56). Austin, TX: Bureau of Economic Geology, University of Texas.

Hayes, M. O. (1979), Barrier island morphology as a function of tidal and wave regime. In Leatherman, S. P. *Barrier Islands, from the Gulf of St. Lawrence to the Gulf of Mexico*. (pp. 1–27). New York: Academic Press.

Hayes, M. O., & FitzGerald, D. M. (2013), Origin, evolution, and classification of tidal inlets. *Journal of Coastal Research*, SI(69), 14–33.

Hapke, C. J., Brenner, O. T., Hehre, R., & Reynolds, B. J. (2013), Coastal change from Hurricane Sandy and the 2012–13 winter storm season—Fire Island, New York: U.S. Geological Survey Open-File Report 2013-1231, 37 p. Reston, VA: U.S Geological Survey.

Héquette, A., Ruz, M.-H., Zemmour, A., Marin, D., Cartier, A., & Sipka, V. (2019), Alongshore Variability in Coastal Dune Erosion and Post-Storm Recovery, Northern Coast of France. *Journal of Coastal Research*, 88(SI), 25–45. https://doi.org/10.2112/SI88-004.1

Hess, K. W., Spargo, E. A., Wong, A., White, S. A., & Gill, S. K. (2005), *VDatum for Central Coastal North Carolina: Tidal Datums, Marine Grids, and Sea Surface Topography* (NOAA Technical Report No. NOS CS 21). Silver Spring, MD: NOAA National Ocean Service.

Himmelstoss, E. A., Henderson, R. E., Kratzmann, M. G., & Farris, A. S. (2018), *Digital Shoreline Analysis System (DSAS) version 5.0 user guide* (USGS Numbered Series No. 2018–1179). *Digital Shoreline Analysis System (DSAS) version 5.0 user guide* (Vol. 2018–1179). Reston, VA: U.S. Geological Survey. https://doi.org/10.3133/ofr20181179

1423 Horton, B. P., Peltier, W. R., Culver, S. J., Drummond, R., Engelhart, S. E., Kemp, A. C., et al.
1424 (2009), Holocene sea-level changes along the North Carolina Coastline and their
1425 implications for glacial isostatic adjustment models. *Quaternary Science Reviews*,
1426 *28*(17), 1725–1736. https://doi.org/10.1016/j.quascirev.2009.02.002

1427 Hosier, P. E., & Cleary, W. J. (1977), Cyclic geomorphic patterns of washover on a barrier
1428 Island in southeastern North Carolina. *Environmental Geology*, 2(1), 23–31.
1429 https://doi.org/10.1007/BF02430662

1430 Hovenga, P. A., Ruggiero, P., Cohn, N., Jay, K. R., Hacker, S. D., Itzkin, M., & Moore, L. (2019),
1431 Drivers of dune evolution in Cape Lookout National Seashore, NC. In *Coastal*
1432 *Sediments 2019* (Vols. 1–0, pp. 1283–1296). World Scientific.
1433 https://doi.org/10.1142/9789811204487_0112

1434 Hoyt, J. H. (1967), Barrier Island Formation. *Geological Society of America Bulletin*, 78(9),
1435 1125. https://doi.org/10.1130/0016-7606(1967)78[1125:BIF]2.0.CO;2

1436 Hudock, J. W., Flaig, P. P., & Wood, L. J. (2014), Washover fans: a modern geomorphologic
1437 analysis and proposed classification scheme to improve reservoir models. *Journal of*
1438 *Sedimentary Research*, *84*(10), 854–865. https://doi.org/10.2110/jsr.2014.64

1439 Inman, D. L., & Dolan, R. (1989), The Outer Banks of North Carolina: Budget of Sediment
1440 and Inlet Dynamics along a Migrating Barrier System. *Journal of Coastal Research*,
1441 *5*(2), 193–237.

1442 Itzkin, M., Moore, L. J., Ruggiero, P., Hacker, S. D., & Biel, R. G. (2021), The relative influence
1443 of dune aspect ratio and beach width on dune erosion as a function of storm
1444 duration and surge level. *Earth Surface Dynamics*, 9(5), 1223–1237.
1445 https://doi.org/10.5194/esurf-9-1223-2021

1446 Jin, D., Hoagland, P., Au, D. K., & Qiu, J. (2015), Shoreline change, seawalls, and coastal
1447 property values. *Ocean & Coastal Management*, *114*, 185–193.
1448 https://doi.org/10.1016/j.ocecoaman.2015.06.025

1449 Jones, B. M., Grosse, G., Hinkel, K. M., Arp, C. D., Walker, S., Beck, R. A., & Galloway, J. P.
1450 (2012), Assessment of pingo distribution and morphometry using an IfSAR derived

digital surface model, western Arctic Coastal Plain, Northern Alaska. *Geomorphology*, *138*(1), 1–14. https://doi.org/10.1016/j.geomorph.2011.08.007

Kranenburg, C.J., Ritchie, A.C., Brown, J.A., Over, J.R., Buscombe, D., Sherwood, C.R., Warrick, J.A., Wernette, P.A., (2020), Post-Hurricane Florence Aerial Imagery: Cape Fear to Duck, North Carolina, October 6-8, 2018: U.S. Geological Survey data release, https://doi.org/10.5066/P91KB9SF

Kranenburg, C.J., Ritchie, A.C., Brown, J.A., Over, J.R., Sherwood, C.R., Warrick, J.A., & Wernette, P.A., (2021a), Aerial imagery of the North Carolina coast: 2019-08-30 and 2019-09-02, pre-Hurricane Dorian U.S. Geological Survey data release, https://doi.org/10.5066/P9WR0VB1

Kranenburg, C.J., Ritchie, A.C., Brown, J.A., Over, J.R., Sherwood, C.R., Warrick, J.A., & Wernette, P.A. (2021b), Aerial imagery of the North Carolina coast: 2019-09-08 to 2019-09-13, post-Hurricane Dorian: U.S. Geological Survey data release, https://doi.org/10.5066/P9TPKMBB

Kranenburg, C.J., Ritchie, A.C., Brown, J.A., Over, J.R., Sherwood, C.R., Warrick, J.A., & Wernette, P.A., (2022a), Aerial imagery of the North Carolina coast: 2019-10-11: U.S. Geological Survey data release, https://doi.org/10.5066/P9RRSMOJ

Kranenburg, C.J., Ritchie, A.C., Brown, J.A., Over, J.R., Sherwood, C.R., Warrick, J.A., & Wernette, P.A. (2022b), Aerial imagery of the North Carolina coast: 2019-11-26: U.S. Geological Survey data release, https://doi.org/10.5066/P99TL46N

Lane, S. N., Westaway, R. M., & Hicks, D. M. (2003), Estimation of erosion and deposition volumes in a large, gravel-bed, braided river using synoptic remote sensing. *Earth Surface Processes and Landforms*, *28*(3), 249–271. https://doi.org/10.1002/esp.483

Lazarus, E. D. (2016), Scaling laws for coastal overwash morphology. *Geophysical Research Letters*, *43*(23), 12,113-12,119. https://doi.org/10.1002/2016GL071213

Lazarus, E. D., Davenport, K. L., & Matias, A. (2020), Dynamic allometry in coastal overwash morphology. *Earth Surface Dynamics*, *8*(1), 37–50. https://doi.org/10.5194/esurf-8-37-2020

1479 Lazarus, E. D., Williams, H., and Goldstein, E. B. (2022), Volume estimation from planform
1480 characteristics of washover morphology. *Geophysical Research Letters*.
1481 https://doi.org/10.1029/2022GL100098

1482 Leatherman, S. P. (1979), Barrier dune systems: A reassessment. *Sedimentary Geology*,
1483 *24*(1), 1–16. https://doi.org/10.1016/0037-0738(79)90025-3

1484 Leatherman, S. P. (1983), Barrier dynamics and landward migration with Holocene sea-
1485 level rise. *Nature*, *301*(5899), 415–417. https://doi.org/10.1038/301415a0

1486 Lennon, G. (1991), The nature and causes of hurricane-induced ebb scour channels on a
1487 developed shoreline. *Journal of Coastal Research*, (8), 13.

1488 Lentz, E. E., Thieler, E. R., Plant, N. G., Stippa, S. R., Horton, R. M., & Gesch, D. B. (2016),

1489 Evaluation of dynamic coastal response to sea-level rise modifies inundation
1490 likelihood. *Nature Climate Change, 6,* 696–700.
1491 https://doi.org/10.1038/nclimate2957.

1492 Liebowitz, D. M., Nielsen, K. J., Dugan, J. E., Morgan, S. G., Malone, D. P., Largier, J. L.,
1493 Hubbard, D. M., & Carr, M. H. (2016), Ecosystem connectivity and trophic subsidies
1494 of sandy beaches. *Ecosphere, 7*, e01503. https://doi.org/10.1002/ecs2.1503.

1495 Little, C. M., Piecuch, C. G., & Ponte, R. M. (2021), North American East Coast Sea Level
1496 Exhibits High Power and Spatiotemporal Complexity on Decadal Timescales.
1497 *Geophysical Research Letters*, *48*(15), e2021GL093675.
1498 https://doi.org/10.1029/2021GL093675

1499 Loreau, M., Mouquet, N., & Holt, R.D. (2003), Meta-ecosystems—a theoretical framework
1500 fora spatial ecosystem ecology. *Ecology Letters*, 6, 673–679.
1501 https://doi.org/10.1046/j.1461-0248.2003.00483.x

1502 Lorenzo-Trueba, J., & Mariotti, G. (2017) Chasing boundaries and cascade effects in a
1503 coupled barrier-marsh-lagoon system. *Geomorphology*, 290, 153–163.
1504 https://doi.org/10.1016/j.geomorph.2017.04.019

1505 Luettich, R. A., Carr, S. D., Reynolds-Fleming, J. V., Fulcher, C. W., & McNinch, J. E. (2002),
1506 Semi-diurnal seiching in a shallow, micro-tidal lagoonal estuary. *Continental Shelf*
1507 *Research*, 22(11), 1669–1681. https://doi.org/10.1016/S0278-4343(02)00031-6

1508 MacKinnon, J. B. 2022. True Grit. *The Atavist* (132). https://magazine.atavist.com/true-grit-
1509 cows-core-banks-hurricane-dorian-survival/

1510 Mallinson, D. J., Culver, S. J., Riggs, S. R., Walsh, J. P., Ames, D., & Smith, C. W. (2008), *Past,*
1511 *Present and Future Inlets of the Outer Banks Barrier Islands, North Carolina* (White
1512 Paper). Department of Geological Sciences, East Carolina University. Retrieved from
1513 https://web.archive.org/web/20111016221534/http://www.ecu.edu/icsp/ICSP/R
1514 eports_files/PastPresentAndFutureInletsDec2008.pdf

1515 Matthews, N. A., Noble, T. A., & Breithaupt, B. H. (2016), Close-range photogrammetry for 3-
1516 D ichnology: the basics of photogrammetric ichnology. In P. L. Falkingham, D. Marty,
1517 & A. Richter (Eds.), *Dinosaur tracks—Next Steps* (p. 520). Bloomington: Indiana
1518 University Press.

1519 McBride, R. A., Anderson, J. B., Buynevich, I. V., Cleary, W., Fenster, M. S., FitzGerald, D. M., et
1520 al. (2013), 10.8 Morphodynamics of Barrier Systems: A Synthesis. In J. F. Shroder
1521 (Ed.), *Treatise on Geomorphology* (pp. 166–244). San Diego: Academic Press.
1522 https://doi.org/10.1016/B978-0-12-374739-6.00279-7

1523 Michaud, K. M., Emery, K. A., Dugan, J. E., Hubbard, D. M., & Miller, R. J. (2019), Wrack
1524 resource use by intertidal consumers on sandy beaches. *Estuarine, Coastal and Shelf*
1525 *Science, 221*, 66–71. https://doi.org/10.1016/j.ecss.2019.03.014

1526 Morton, R. A., & Miller, T. (2005), *National Assessment Of Shoreline Change: Part 2, Historical*
1527 *Shoreline Changes And Associated Coastal Land Loss Along The U.S. Southeast Atlantic*
1528 *Coast* U.S. Geological Survey, Open-File Report No. 2005–1401 (p. 35). Reston, VA:
1529 U.S Geological Survey.

1530 Morton, R. A., & Paine, J. G. (1985). Beach and vegetation - line changes at Galveston Island,
1531 Texas: erosion, deposition, and recovery from Hurricane Alicia. [Monograph or
1532 Serial Issue]. Retrieved April 28, 2021, from http://aquaticcommons.org/14177/

1533 Morton, R. A., & Sallenger Jr., A. H. (2003), Morphological Impacts of Extreme Storms on
1534 Sandy Beaches and Barriers. *Journal of Coastal Research*, 19(3), 15.

1535 Mulhern, J. S., Johnson, C. L., & Martin, J. M. (2017), Is barrier island morphology a function
1536 of tidal and wave regime? *Marine Geology*, *387*, 74–84.
1537 https://doi.org/10.1016/j.margeo.2017.02.016

1538 Mulligan, R. P., Walsh, J. P., & Wadman, H. M. (2015), Storm surge and surface waves in a
1539 shallow lagoonal estuary during the crossing of a hurricane. *Journal of Waterway,*
1540 *Port, Coastal, and Ocean Engineering*, 141(4), A5014001.
1541 https://doi.org/10.1061/(ASCE)WW.1943-5460.0000260

1542 National Geodetic Survey (NGS), (2022), 2019 NOAA NGS Emergency Response Imagery:
1543 Hurricane Dorian, https://www.fisheries.noaa.gov/inport/item/57856, accessed
1544 September 9, 2022.

1545 Natural Resources Conservation Service (NRCS). (2000), Shorebirds: fish and wildlife
1546 habitat management leaflet number 17. U.S. Department of Agriculture. 14 pp.
1547 Accessed June 15, 2020 at
1548 https://directives.sc.egov.usda.gov/OpenNonWebContent.aspx?content=18480.wba

1549 Neuendorf, K. K. E., Mehl Jr., J. P., & Jackson, J. A. (2011). *Glossary of Geology* (Fifth Edition,
1550 Revised). American Geosciences Institute.

1551 Nienhuis, J. H., & Ashton, A. D. (2016), Mechanics and rates of tidal inlet migration:
1552 Modeling and application to natural examples. *Journal of Geophysical Research:*
1553 *Earth Surface*, *121*(11), 2118–2139. https://doi.org/10.1002/2016JF004035

1554 Nienhuis, J. H., & Lorenzo-Trueba, J. (2019), Can Barrier Islands Survive Sea-Level Rise?
1555 Quantifying the Relative Role of Tidal Inlets and Overwash Deposition. *Geophysical*
1556 *Research Letters*, *46*(24), 14613–14621. https://doi.org/10.1029/2019GL085524

1557 Over, J. R., Brown, J. A., Sherwood, C. R., Hegermiller, C. A., Wernette, P. A., Ritchie, A. C., &
1558 Warrick, J. A. (2021a), A survey of storm-induced seaward-transport features
1559 observed during the 2019 and 2020 hurricane seasons. *Shore & Beach*, *89*(2), 31–40.

1560 Over, J. R., Ritchie, A. C., Kranenburg, C. J., Brown, J. A., Buscombe, D., Noble, T., et al.
1561 (2021b), *Processing Coastal Imagery With Agisoft Metashape Professional Edition,*
1562 *Version 1.6—Structure From Motion Workflow Documentation* (Open-File Report No.
1563 2021–1039). Reston, VA: U.S. Geological Survey. Retrieved from
1564 https://pubs.usgs.gov/of/2021/1039/ofr20211039.pdf

1565 Passeri, D. L., Long, J. W., Plant, N. G., Bilskie, M. V., & Hagen, S. C. (2018), The influence of
1566 bed friction variability due to land cover on storm-driven barrier island
1567 morphodynamics. *Coastal Engineering*, 132, 82–94.
1568 https://doi.org/10.1016/j.coastaleng.2017.11.005

1569 Peng, M., Xie, L., & Pietrafesa, L. J. (2004). A numerical study of storm surge and inundation
1570 in the Croatan–Albemarle–Pamlico Estuary System. Estuarine, Coastal and Shelf
1571 Science, 59(1), 121–137. https://doi.org/10.1016/j.ecss.2003.07.010

1572 Perry, M., & Uhler, F. (1988), Food habits and distribution of wintering canvasbacks, *Aythya*
1573 *valisineria*, on Chesapeake Bay. *Estuaries*, *11*, 57–67.

1574 Perry, M. C., Wells-Berlin, A. M, Kidwell, D. M., & Osenton, P. C. (2007), Temporal changes of
1575 populations and trophic relationships of wintering diving ducks in Chesapeake Bay.
1576 *Waterbirds, 30*, 4–16. https://doi.org/10.1675/1524-
1577 4695(2007)030[0004:TCOPAT]2.0.CO;2

1578 Pierce, J. W. (1970), Tidal Inlets and Washover Fans. *The Journal of Geology*, *78*(2), 230–
1579 234. https://doi.org/10.1086/627504

1580 Pietrafesa, L. J., Xie, L., Morrison, J., Janowitz, G. S., Pelissier, J., Keeter, K., & Neuherz, R. A.
1581 (1997), Numerical modelling and computer visualization of the storm surge in and
1582 around the Croatan-Albemarle-Pamlico estuary system produced by hurricane
1583 Emily of August 1993. *MAUSAM*, 48(4), 567–578.
1584 https://doi.org/10.54302/mausam.v48i4.4323

1585 Priestas, A. M., & Fagherazzi, S. (2010), Morphological barrier island changes and recovery
1586 of dunes after Hurricane Dennis, St. George Island, Florida. *Geomorphology*, 114(4),
1587 614–626. https://doi.org/10.1016/j.geomorph.2009.09.022

1588 Riggs, S. R., & Ames, D. V. (2007), *Effect of Storms on Barrier Island Dynamics, Core Banks,*
1589 *Cape Lookout National Seashore, North Carolina, 1960-2001* (Scientific Investigations
1590 Report No. 2006–5309) (p. 73). Reston, VA: U.S. Geological Survey.

1591 Ritchie, A.C., Over, J.R., Kranenburg, C.J., Brown, J.A., Buscombe, D., Sherwood, C.R., Warrick,
1592 J.A., &, P.A (2021), Aerial photogrammetry data and products of the North Carolina
1593 coast—2018-10-06 to 2018-10-08, post-Hurricane Florence: U.S Geological Survey
1594 data release, https://doi.org/10.5066/P9CA3D8P

1595 Ritchie, A.C., Over, J.R., Kranenburg, C.J., Brown, J.A., Buscombe, D., Sherwood, C.R., Warrick,
1596 J.A., and Wernette, P.A, (2022), Aerial photogrammetry data and products of the
1597 North Carolina coast: U.S Geological Survey data release,
1598 https://doi.org/10.5066/P9K3TWY7

1599 Robinson, S., Fraser, J., Catlin, D., Karpanty, S., Altman, J., Boettcher, R., et al. (2019),
1600 Irruptions: evidence for breeding season habitat limitation in Piping Plover
1601 (Charadrius melodus). *US Army Corps of Engineers*. Retrieved from
1602 https://digitalcommons.unl.edu/usarmyceomaha/177

1603 Rolstad, C., Haug, T., & Denby, B. (2009), Spatially integrated geodetic glacier mass balance
1604 and its uncertainty based on geostatistical analysis: application to the western
1605 Svartisen ice cap, Norway. *Journal of Glaciology*, *55*(192), 666–680.
1606 https://doi.org/10.3189/002214309789470950

1607 Russell, P. E. (1993), Mechanisms for beach erosion during storms. *Continental Shelf*
1608 *Research*, 13(11), 1243–1265. https://doi.org/10.1016/0278-4343(93)90051-X

1609 Safak, I., Warner, J. C., & List, J. H. (2016), Barrier island breach evolution: Alongshore
1610 transport and bay-ocean pressure gradient interactions. *Journal of Geophysical*
1611 *Research: Oceans*, 121(12), 8720–8730. https://doi.org/10.1002/2016JC012029

1612 Sallenger Jr., A. H., & Jr. (2000), Storm Impact Scale for Barrier Islands. *Journal of Coastal*
1613 *Research*, 16(3), 890–895.

1614 Sallenger, A. H., Stockdon, H. F., Fauver, L., Hansen, M., Thompson, D., Wright, C. W., &
1615 Lillycrop, J. (2006), Hurricanes 2004: An overview of their characteristics and

1616 coastal change. *Estuaries and Coasts*, 29(6), 880–888.
1617 https://doi.org/10.1007/BF02798647

1618 Sánchez-Arcilla, A., & Jiménez, J. A. (1994), Breaching in a wave-dominated barrier spit: The
1619 Trabucador Bar (north-eastern Spanish coast). *Earth Surface Processes and*
1620 *Landforms*, *19*(6), 483–498. https://doi.org/10.1002/esp.3290190602

1621 Sellars, J. D. & Jolls, C. L. (2007), Habitat modeling for *Amaranthus pumilus:* an application of
1622 light detection and ranging (LiDAR) data. *Journal of Coastal Research, 23*, 1193-1202.
1623 https://doi.org/10.2112/04-0334.1

1624 Sheaves, M. (2009), Consequences of ecological connectivity—the coastal ecosystem
1625 mosaic *Marine Ecology Progress Series, 391,* 107–115.
1626 https://doi.org/10.3354/meps08121.

1627 Sherwood, C. R., Long, J. W., Dickhudt, P. J., Dalyander, P. S., Thompson, D. M., & Plant, N. G.
1628 (2014), Inundation of a barrier island (Chandeleur Islands, Louisiana, USA) during a
1629 hurricane: Observed water-level gradients and modeled seaward sand transport.
1630 *Journal of Geophysical Research: Earth Surface*, 119(7), 2013JF003069.
1631 https://doi.org/10.1002/2013JF003069

1632 Sherwood, C. R., Warrick, J. A., Hill, A. D., Ritchie, A. C., Andrews, B. D., & Plant, N. G. (2018),
1633 Rapid, Remote Assessment of Hurricane Matthew Impacts Using Four-Dimensional
1634 Structure-from-Motion Photogrammetry. *Journal of Coastal Research*, 1303–1316.
1635 https://doi.org/10.2112/JCOASTRES-D-18-00016.1

1636 Short, A. D., & Hesp, P. A. (1982), Wave, beach and dune interactions in southeastern
1637 Australia. *Marine Geology*, 48(3), 259–284. https://doi.org/10.1016/0025-
1638 3227(82)90100-1

1639 Sopkin, K. L., Stockdon, H. F., Doran, K. S., Plant, N. G., Morgan, K. L. M., Guy, K. K., & Smith, K.
1640 E. L. (2014), *Hurricane Sandy: Observations and Analysis of Coastal Change* (USGS
1641 Numbered Series No. 2014–1088) (p. 64). Reston, VA: U.S. Geological Survey.
1642 Retrieved from http://pubs.er.usgs.gov/publication/ofr20141088

1643 Soulsby, R. L. (1997), *Dynamics of Marine Sands* (Vols. 1–0). Thomas Telford Publishing.
1644 https://doi.org/10.1680/doms.25844.fm

1645 Splinter, K. D., & Palmsten, M. L. (2012), Modeling dune response to an East Coast Low.
1646 *Marine Geology*, *329–331*, 46–57. https://doi.org/10.1016/j.margeo.2012.09.005

1647 Splinter, K. D., Kearney, E. T., & Turner, I. L. (2018), Drivers of alongshore variable dune
1648 erosion during a storm event: Observations and modelling. *Coastal Engineering*, *131*,
1649 31–41. https://doi.org/10.1016/j.coastaleng.2017.10.011

1650 Stockdon, H. F., Holman, R. A., Howd, P. A., & Sallenger, A. H. (2006), Empirical
1651 parameterization of setup, swash, and runup. *Coastal Engineering*, *53*(7), 573–588.
1652 https://doi.org/10.1016/j.coastaleng.2005.12.005

1653 Stockdon, H. F., Sallenger, A. H., Holman, R. A., & Howd, P. A. (2007), A simple model for the
1654 spatially-variable coastal response to hurricanes. *Marine Geology*, 238(1), 1–20.
1655 https://doi.org/10.1016/j.margeo.2006.11.004

1656 Stone, G. W., & McBride, R. A. (1998), Louisiana Barrier Islands and Their Importance in
1657 Wetland Protection: Forecasting Shoreline Change and Subsequent Response of
1658 Wave Climate. *Journal of Coastal Research*, *14*(3), 900–915.

1659 Taylor, J. R. (1997), *An Introduction to Error Analysis*. California: University Science Books.

1660 Thoeni, K., Giacomini, A, Murtagh, R., & Kniest, E. (2014), A comparison of multi-view 3D
1661 reconstruction of a rock wall using several cameras and a laser scanner. *The*
1662 *International Archives of the Photogrammetry, Remote Sensing and Spatial*
1663 *Information Sciences, Volume XL-5, 2014 ISPRS Technical Commission V Symposium,*
1664 *23 – 25 June 2014, Riva Del Garda, Italy*.

1665 van de Koppel, J., van der Heide, T., Altieri, A. H., Eriksson, B. K., Bouma, T. J., Olff, H., &
1666 Silliman, B. R. (2015), Long-distance interactions regulate the structure and
1667 resilience of coastal ecosystems. *Annual Review of Marine Science, 7*, 139–158.
1668 https://doi.org/10.1146/annurev-marine-010814-015805.

1669 Van der Lugt, M. A., Quataert, E., van Dongeren, A., van Ormondt, M., & Sherwood, C. R.
1670 (2019), Morphodynamic modeling of the response of two barrier islands to Atlantic

hurricane forcing. *Estuarine, Coastal and Shelf Science*, 229, 106404. https://doi.org/10.1016/j.ecss.2019.106404

Vellinga, P. (1982), Beach and dune erosion during storm surges. *Coastal Engineering*, *6*(4), 361–387. https://doi.org/10.1016/0378-3839(82)90007-2

Walters, D. C. & Kirwan, M. L. (2016), Optimal hurricane overwash thickness for maximizing marsh resilience to sea level rise. *Ecology and Evolution, 6*, 2948–2956. https://doi.org/10.1002/ece3.2024

Warrick, J. A., Ritchie, A. C., Adelman, G., Adelman, K., & Limber, P. W. (2017), New Techniques to Measure Cliff Change from Historical Oblique Aerial Photographs and Structure-from-Motion Photogrammetry. *Journal of Coastal Research*, *33*(1), 39–55. https://doi.org/10.2112/JCOASTRES-D-16-00095.1

Wei, E., & Miselis, J. (2022), Geologic Framework, Anthropogenic Impacts, and Hydrodynamics Contribute to Variable Sediment Availability and Shoreface Morphology at the Rockaway Peninsula, NY. *Journal of Marine Science and Engineering*, 10(7), 989. https://doi.org/10.3390/jmse10070989

Wells, J. T., & McNinch, J. (1991), Beach Scraping in North Carolina with Special Reference to its Effectiveness During Hurricane Hugo. *Journal of Coastal Research*, 249–261.

Wolinsky, M. A., & Murray, A. B. (2009), A unifying framework for shoreline migration: 2. Application to wave-dominated coasts. *Journal of Geophysical Research: Earth Surface*, *114*(F1). https://doi.org/10.1029/2007JF000856

Young, A. P., Flick, R. E., Gallien, T. W., Giddings, S. N., Guza, R. T., Harvey, M., et al. (2018), Southern California Coastal Response to the 2015–2016 El Niño. *Journal of Geophysical Research: Earth Surface*, *123*(11), 3069–3083. https://doi.org/10.1029/2018JF004771

Zeigler, S. L., Gutierrez, B. T., Sturdivant, E. J., Catlin, D. H., Fraser, J. D., Hecht, A., et al. (2019), Using a Bayesian network to understand the importance of coastal storms and undeveloped landscapes for the creation and maintenance of early successional

habitat. *PLOS ONE*, *14*(7), e0209986. https://doi.org/10.1371/journal.pone.0209986

Zeigler, S. L., Gutierrez, B. T., Hecht, A., Plant, N. G., & Sturdivant, E. J. (2021), Piping plovers demonstrate regional differences in nesting habitat selection patterns along the U.S. Atlantic coast. *Ecosphere*, 12(3), e03418. https://doi.org/10.1002/ecs2.3418

Zhang, K., Whitman, D., Leatherman, S., & Robertson, W. (2005), Quantification of Beach Changes Caused by Hurricane Floyd Along Florida's Atlantic Coast Using Airborne Laser Surveys. *Journal of Coastal Research*, 21(1 (211)), 123–134. https://doi.org/10.2112/02057.1